energies

MDPI

Article

Architectural Vulnerability Mapping and Analysis in Hybrid AC/DC Distribution Networks

Krishna Kumar [1], Ramesh Rayudu [2], Aleksandra Lekić [3], Tek Tjing Lie [4] and Nirmal-Kumar C. Nair [1,*]

[1] Department of ECSE, The University of Auckland, Auckland 1010, New Zealand; krishna.kumar@auckland.ac.nz
[2] School of ECS, Victoria University of Wellington, Wellington 6012, New Zealand; ramesh.rayudu@vuw.ac.nz
[3] Faculty of EEMCS, Delft University of Technology, 2628 CD Delft, The Netherlands; a.lekic@tudelft.nl
[4] Department of EEE, Auckland University of Technology, Auckland 1010, New Zealand; tek.lie@aut.ac.nz
* Correspondence: n.nair@auckland.ac.nz

Abstract

The growing integration of distributed renewable resources is pushing medium-voltage distribution grids toward hybrid AC/DC configurations, whose topology-dependent vulnerabilities, including harmonic resonance, sub-synchronous & converter-control interactions (SSCI/CCI), AC/DC interface faults, and protection miscoordination, remain poorly addressed. This paper develops a vulnerability mapping framework for hybrid MVAC/MVDC systems that combines multilayer network topology modelling, multi-source harmonic-domain analysis using frequency coupling matrices, and Backward-Forward Sweep power flow. The relationship between topology, resonant-mode count, and SSCI phase-margin coupling is derived analytically from the admittance matrix. The framework is applied to 12 configurations across four topologies, using phasor-domain simulation with electromagnetic transient (EMT) verification of fault and converter cases. The results show that, for an XLPE 95 mm^2 DC cable, the dominant resonance falls below 200 Hz for feeders longer than about 12.6 km; Monte Carlo analysis places this crossing at 10.0–14.2 km (5th–95th percentile). At 60% renewable penetration, four configurations (C5, C8, C9, C12) exceed the unity resonance-vulnerability threshold, and the meshed DC-side grid-forming configuration (C8) violates the 30° phase-margin limit. Because the penetration at which this limit is lost ranges from 20% to 85%, grid-forming deployment should rely on configuration-specific impedance and phase-margin assessment rather than a universal threshold. Overcurrent relays misoperate in 31–61% of DC pole-to-ground faults, reflecting a mismatch between magnitude-based protection and DC fault signatures under high-impedance grounding. A long short-term memory (LSTM) classifier trained on 468 simulated scenarios achieves 94.4% accuracy on 120 held-out scenarios under noise-free conditions, but its RVI, SVI, and FPSS accuracy fall to 42.5–50.8% when the meshed topology class is withheld, so each topology class must be represented in the training data.

Keywords: hybrid networks; harmonic analysis; sub-synchronous control interaction; converter-control interaction; architectural vulnerability; power system analysis; protection coordination

Check for updates

Academic Editor: Stefano Rinaldi

Received: 14 August 2026
Revised: 30 October 2026
Accepted: 3 November 2026
Published: 7 November 2026

Copyright: © 2026 by the authors. Licensee MDPI, Basel, Switzerland. This article is an open access article distributed under the terms and conditions of the Creative Commons Attribution (CC BY) license.

1. Introduction

Medium-voltage distribution networks are facing a fundamental shift in their structure due to the incorporation of large-scale distributed sources such as photovoltaic (PV) power generation, battery energy storage, EV infrastructure, and loads associated with data centers,

all of which operate at DC voltages. The combined pressures have led to a movement towards hybrid MVAC/MVDC architectures in which the AC and DC portions of the network share the same geographical area and are linked via voltage-source converters (VSCs). The advantages of using DC segments include the elimination of losses due to reactive components in underground cables, direct interfacing of PV sources and battery storage systems without the need for inversion stages, and improved power-flow control that is not possible with purely passive AC transformers [1–4].

In New Zealand's context, high renewable penetration targets, geographically dispersed generation, and long rural feeders create conditions favorable to hybrid architecture [5]. The power-electronic interfaces that make hybrid AC/DC networks attractive also introduce four inter-related dynamic vulnerabilities unfamiliar to AC distribution engineers: harmonic resonance amplification, whereby the high shunt capacitance of DC cables lowers the network resonant frequencies into inverter control frequency bands [6,7]; sub-synchronous control interaction (SSCI) and its above-fundamental counterpart, converter-control interaction (CCI), low-frequency forms of harmonic resonance whereby grid-forming inverter control dynamics interact with DC-network resonances in or near the sub-synchronous band; DC fault propagation, whereby capacitor discharge currents reach high values on the microsecond scale, do not have a natural zero crossing, and propagate across AC/DC boundaries both physically and through control mechanisms [8]; and finally protection coordination failure, whereby relay design, based on AC faults, fails when DC system modifications change the fault current environment [6]. The four mechanisms are interrelated, and each mechanism will be discussed with the purpose-designed quantitative tools: admittance matrix derivation of topology-dependent resonance; multi-source frequency coupling matrix extension of harmonic domain analysis; Backward-Forward Sweep power flow solver verified to 0.013%; phasor-domain fault simulation supported by EMT checks; and a machine-learning classifier for real-time vulnerability classification.

Notably, much of the extant literature on these failure modes is considered separately. Harmonic analysis of standalone converters is thoroughly documented [9]; sub-synchronous resonance in wind farms connected through series-compensated AC lines has been thoroughly investigated [10]; and the protection of DC microgrids is actively researched [11]. However, the architectural aspects of how the selection of network architecture, renewable power integration method, controller hierarchies, and protection zones jointly define the composite vulnerability profile across all phenomena have not yet been considered.

The current work attempts to address this gap by introducing a framework to map architectural vulnerabilities in hybrid MVAC/MVDC distribution networks. Three analytical approaches form the basis of the introduced framework: the MLN topology modeling approach proposed by Cuppen et al. [5]; the generalized harmonic domain analysis proposed by Schipper et al. [12]; and the steady-state power system analysis methodology proposed by Schipper et al. [13]. Real-time operational vulnerability monitoring is accomplished through the inclusion of a machine learning classification layer in the developed framework, where three supervised learning models, such as gradient-boosted trees (XGBoost), multilayer perceptron (MLP), and long short-term memory network (LSTM), are trained on 468 labeled scenarios generated from 240 fault simulations, 48 harmonic-domain analyses, and 180 normal-operation time-domain simulations. The main contributions of this paper are as follows:

(i) Analytical link between topology and resonance/SSCI vulnerability: Starting from the network admittance matrix, closed-form conditions are derived that relate the topology (radial, ring, meshed, hybrid overlay) to the number and degeneracy

of resonance modes, and to the coupling of SSCI phase margins among multiple grid-forming sources.

(ii) Multi-source harmonic-domain analysis: The single-source harmonic-domain method of [12] is extended to multiple distributed sources using full frequency coupling matrices.

(iii) Four quantitative vulnerability indices with stated thresholds: RVI, SVI, FPSS, and CCS are defined, with thresholds and their provenance. They are evaluated for 12 configurations, spanning 4 topologies, 3 source placements, and 4 control strategies, across all 4 vulnerability classes simultaneously.

(iv) Design limits supported by sensitivity analysis: These include a cable-length criterion for keeping the dominant resonance above 200 Hz (about 12.6 km at nominal parameters and about 10 km at 95% confidence for XLPE 95 mm^2 cable, and 9–21 km for 150–350 nF/km cables), tested with tolerance and Monte Carlo analysis.

(v) A simulation-trained vulnerability classifier: Conventional supervised models (XGBoost, MLP, and LSTM) are trained on 468 simulated scenarios to estimate the class of all four indices from standard power-quality measurements. They are tested for out-of-distribution, leave-one-configuration-out, and leave-one-topology-out generalization, as well as robustness to measurement noise and communication dropout.

(vi) Five architectural planning principles distilled from these results: Compared with the multilayer-network framework of [5], which describes, and with the harmonic-domain [12] and steady-state [13] methods, which analyze individual power flow, the present work combines these tools into a single framework that ranks complete hybrid architectures across all four vulnerability classes.

The rest of the paper is structured as follows: Section 2 reviews literature background and discusses the literature gaps to be targeted, Section 3 discusses the architectural design space, Section 4 formulates the vulnerability taxonomy along with the corresponding quantitative metrics, Sections 5–8 discuss the simulation approach and its outcomes for each type of vulnerability, Section 9 discusses the ML classifier, Section 10 summarizes the outcomes, states the scope and limitations, reports additional verification studies, and draws architectural guidelines, and Section 11 concludes the paper.

2. Background and Related Work

2.1. MVDC Distribution

MVDC distribution systems' engineering fundamentals are best understood through CIGRE Technical Brochure 793 [6], which identifies the key unsolved problems as grounding, protection, control coordination, and simulation methodology. Another benchmarking source relevant to the topic is the Horizon 2020 EASY-RES project, which was dedicated to the development of KPI-based performance assessments for ancillary services in a network with a high level of renewable energy integration, which were tested on the CIGRE European MV benchmark (TB 575) and CIGRE LV benchmark networks [14]. Even though EASY-RES has been designed specifically to enable ancillary services in an AC network, its reliance on the same CIGRE benchmarking infrastructure makes its results comparable to those of this work, which, however, covers hybrid MVAC/MVDC distribution systems.

2.2. Harmonic Analysis in Converter-Dominated Networks

The harmonic analysis of converter-dominated power systems is conducted within the harmonic-domain formulation first introduced by Arrillaga et al. [15,16], in which nonlinear elements are modelled as Norton equivalents using frequency-coupled matrices. This method was further developed by Schipper et al. [12] to account for devices exhibiting memory effects, such as magnetic hysteresis in transformers. The formulation has not yet

been extended to networks with many harmonically excited elements that interact through the impedance network, as required for hybrid MVAC/MVDC systems.

2.3. Sub-Synchronous Control Interaction and Impedance-Based Stability

The sub-synchronous control interaction (SSCI) problem was first identified for type-3 wind farms operating on series-compensated AC transmission lines [17], where SSCI arises from the coupling between the rotor-side converter dynamics and the electrical resonance introduced by series capacitors. Sun [18] proposed an impedance-based stability criterion for grid-connected inverters that extends Middlebrook's input-filter criterion, and it has since been applied to VSC-HVDC and MMC-HVDC systems [19,20]. A lot of development has occurred since then; in particular, computational platforms have been developed to perform impedance-based stability analysis for hybrid AC/DC systems [21–24], and numerous publications have addressed multi-converter and grid-forming inverter configurations [25]. However, the interaction mechanism in the hybrid MVAC/MVDC system differs significantly from that in the classical SSCI scenario, as DC cable capacitance becomes a new source of resonance. At the same time, the inverter control loops, with bandwidths of tens to hundreds of hertz, replace the rotor-side converter current controller in interactions with the resonance.

The extension of impedance-based analysis to multi-inverter hybrid systems with various control schemes is not addressed in the existing literature. Recently, some developments have been achieved in the field of grid-forming stability analysis and multi-inverter dynamics analysis, such as a comprehensive study on transient stability enhancement techniques for grid-forming converters [26], a multi-loop droop control stability analysis with current limiters [27], and a comparative study on grid-forming and grid-following dynamics in combination transmission-distribution systems [28].

2.4. DC Network Protection

DC grid protection faces an essential problem. Fault currents generated by cable and converter capacitances reach their peak within microseconds and lack any zero-crossing point, thereby requiring a technology capable of responding at speeds several times those of AC protection [29–31]. Co-ordination across boundaries, where a fault in one zone should not lead to unnecessary tripping in another, requires communication-based approaches more advanced than conventional radial feeder protection. The latest developments in this field include a protection concept for MVDC networks with network reconfiguration [32], a review of fault detection techniques in MVDC networks [33], and a setting-less, threshold-less fault detection technique for the DC grid [34].

2.5. Machine Learning for Vulnerability Assessment

The application of machine learning algorithms in power system fault classification, stability evaluation, and harmonic source localization [35–39] has been explored; however, their use for architectural-level vulnerability assessment in hybrid AC/DC systems has not been sufficiently examined. This work provides insight into the ability of machine learning algorithms to classify the vulnerability state of a hybrid MVAC/MVDC system, considering harmonic, oscillatory, and fault-propagation aspects, using only standard power-quality measurements. Recent surveys on machine learning applications in power system protection and emergency control [40,41] provide a broader methodological context and transfer learning approaches for online assessments of security and stability [42,43].

3. Architectural Design Space for Hybrid MVAC/MVDC Networks

3.1. Topology Architecture

According to the multilayer network (MLN) framework [5] by Cuppen et al., the network structure can be classified into elementary layers (voltage levels and types), nodes (sets of bus equipment), and edges (intra-layer conductors and inter-layer converters). Four topologies are described here. The radial DC topology places one AC/DC converter at the head of the DC feeder, with renewable energy and loads connected in a radial configuration. This kind of simplicity in topology provides a well-defined protection zone, unidirectional power flow, and a single resonant frequency determined by the feeder's total inductance and cable capacitance. The major problem with this type of topology lies in the system's architectural dependence on the head-end converter. In a DC Ring Topology, the DC network is connected to two AC/DC converters, providing redundancy by creating two paths and thus eliminating the risk of total isolation in the event of a converter failure. The availability of two converters, each with a different impedance response due to different control policies, determines the network's resonant frequency.

The meshed DC topology extends the ring configuration to include multiple DC buses and AC feeder connections, providing maximum flexibility, albeit at the expense of significantly increased complexity in protection coordination and resonant-condition analysis. The hybrid overlay topology involves placing DC segments within a preexisting MVAC infrastructure by installing converters at carefully selected locations. This is the most economically viable route in the near future, but retains the same resonant characteristics as the existing AC network and the new DC cables.

3.2. Source Architecture

The spatial configuration of the connections between renewable sources and the connecting points plays a significant role in determining the harmonic interaction picture. In situations when sources are connected only to the AC part of the grid, then the DC side acts as the path of the power flow, and harmonic currents generated by inverters of renewable sources pass through the impedance map of the network, which is created but not supplied with electricity through the DC grid infrastructure. When sources are connected to the DC bus, as in large PV farms and batteries, the current generated by switching interacts with the DC grid's cable capacitance, causing resonance effects distinct from those on the AC side.

3.3. Control Architecture

The principal control approach is the primary factor determining vulnerability to oscillations. The grid-following inverters with control based on the phase-locked loop (PLL) operate as current sources synchronized with the grid, producing harmonics primarily determined by the switching frequency and LCL filter design. They provide a very low intrinsic vulnerability in isolation, although they cannot generate network voltage without synchronous control. The droop-controlled converters control their active/reactive power by monitoring frequency and voltage differences, resulting in frequency-dependent impedances at their terminals that can lead to resonance with the network under certain conditions. More than one droop-controlled converter connected to the same DC-bus may exhibit oscillatory behavior due to the DC-bus impedance.

Grid-forming inverters generate their own voltage references with low-impedance (voltage-source) terminal characteristics. Typically, the outer voltage control bandwidths for grid-forming inverters are 10–100 Hz and include the sub-synchronous resonance range caused by MVDC cable capacitance. While grid-forming control is increasingly regarded as

essential for 100% renewable power systems, it presents the most complex vulnerability landscape among all approaches.

A fourth control-based variation, and one of increasing importance, is the dual-port grid-forming (DP-GFM) control scheme, in which one single converter controls both the AC and DC bus voltages in a coordinated fashion via its inner loops [44]. Dual-port grid-forming converters exhibit a unique vulnerability due to interactions between the two control loops, arising from the need for dual-voltage regulation. In Table 1, 'Mixed' control denotes grid-forming DC-side sources with grid-following AC-side sources.

Table 1. Twelve evaluated architectural configurations.

Config	Topology	Source Placement	Control Strategy
C1	Radial	AC-side	Grid-following
C2	Radial	DC-side	Grid-following
C3	Radial	Mixed	Droop
C4	Ring	AC-side	Grid-following
C5	Ring	DC-side	Grid-forming
C6	Ring	Mixed	Mixed
C7	Meshed	AC-side	Grid-forming
C8	Meshed	DC-side	Grid-forming
C9	Meshed	Mixed	Mixed
C10	Hybrid overlay	AC-side	Grid-following
C11	Hybrid overlay	DC-side	Droop
C12	Hybrid overlay	Mixed	Mixed

3.4. Protection Architecture

The design of protection zones needs to consider three different types of fault current characteristics: normal AC fault currents that include natural zero crossings, DC capacitor discharge fault current with microseconds rise time and no zero crossings at all, and fault contribution from the converters, being equal to 1.0–1.2 per unit of rated current only. Different detection and interruption principles are required for each type. The placement of protection zone boundaries relative to AC/DC converter installation locations is thus the primary architectural factor affecting vulnerability to protection coordination. The inverter current limiters, which limit the output fault current to 1.0–1.2 pu of the rated current over a 5 ms period, are another important architectural design component, since they change the source impedance as perceived by the upstream protective devices. As a result, fault current signatures become indistinguishable from those of a heavy load, necessitating modelling of the current limiter.

3.5. Evaluated Configuration Matrix

In this paper, 12 architectural configurations are evaluated. They form a subset of the 48 possible combinations of four topologies, three source placements, and four control strategies (grid-following, droop, grid-forming, and mixed), chosen so that each topology is represented by three configurations spanning its design space. In each topology group, source location and control system vary together rather than separately.

4. Vulnerability Taxonomy and Classification Framework

Vulnerability in architectural design is the characteristic of a network topology that reflects how prone the architecture is to undesirable operational outcomes across all operational scenarios. The definition does not consider component reliability; rather, it focuses on emergent behavior arising from the arrangement of components within a specific topology and control structure. Four classes of vulnerabilities depend on different physical mechanisms.

4.1. Vulnerability Class 1: Harmonic Resonance Instability

Resonance vulnerability arises because the frequency components of distributed energy sources fall within the same range as the system impedance's resonant frequency. For passive systems, the voltage magnification will be bounded. In contrast, for active systems with inverter-interfaced distributed energy sources, the resonant overvoltage feedback to the inverter creates a positive feedback phenomenon in which the bounded oscillations become unbounded. The formula for calculating the Resonance Vulnerability Index (RVI) is shown in Equation (1).

$$RVI\ (f) = |Z_{net}(f)\ .\ Y_{src}(f)|, \quad RVI = max_f\ RVI(f) \tag{1}$$

Resonance vulnerability index (RVI) is the size of the minor-loop gain without dimension defined through the network driving-point impedance and the aggregate output admittance of the inverter source at each harmonic frequency, where $Z_{net}(f)[\Omega]$ is the Thevenin equivalent driving-point impedance of the network viewed from the harmonic injection point. In contrast, $Y_{src}(f) = \frac{I_{inj}(f)}{V(f)}$ [S] is the effective aggregate admittance of the inverter sources connected to this point at harmonic frequency f. Since the multiplication of $Z_{net}(f)\ .\ Y_{src}(f)$ is dimensionless ($\Omega \times S = 1$), the RVI criterion fits the minor-loop-gain representation of the generalized Nyquist/impedance-stability criterion (Middlebrook; Sun [18]; Xu & Fan [19]): the combined network-source system is guaranteed to be small-signal stable, if the plot of $Z_{net}(f)\ .\ Y_{src}(f)$ doesn't encircle the point $(-1, j0)$ in the complex plane. RVI > 1 is a necessary, but not sufficient, condition for such an encirclement: instability additionally requires the loop phase to reach $-180°$ at a frequency where the loop-gain magnitude exceeds unity. RVI is therefore read together with SVI, which captures the phase condition.

4.2. Vulnerability Class 2: Sub-Synchronous and Converter-Control Interactions

Two related interaction regimes are distinguished in this paper. Sub-synchronous control interaction (SSCI) denotes an interaction between converter controls and the network in which the resonant frequency lies below the fundamental frequency ($f < 50$ Hz) in this system. Converter-control interaction (CCI), also referred to here as an SSCI-type interaction, denotes the same impedance/control mechanism: a network resonance coinciding with a low phase margin of the converter loop, when the frequency lies above the fundamental but inside the converter-control bandwidth. Both are specific forms of harmonic resonance susceptibility and are assessed using the same phase-margin-based index (SVI). The concept of sub-synchronous oscillation is generally defined in the context of power systems as energy exchange between the electrical grid and generation/converter devices at a frequency below the system's fundamental frequency [45,46]. In a 50 Hz system, it covers all frequencies below 50 Hz without a specific lower bound; field observations indicate that SSCI occurs even at frequencies as low as 3.5–4 Hz [46]. The critical interaction band depends on the configuration itself because it is defined by the specific values of total inductance and capacitance (Equation (10)) and the VSC control bandwidths for each configuration, rather than by a fixed range. For the nominal values of the VSC parameters, the interaction band

falls within the approximate range of 5–45 Hz for the radial and ring configuration; for the meshed configuration with grid-forming sources on the DC side (C8), the longer exposed cable length and the additional parallel converter path shift the dominant control-interaction resonance up to about 83 Hz. Because 83 Hz lies above the 50 Hz fundamental, this mode is not a sub-synchronous interaction in the strict sense. It is a converter-control interaction (CCI): it lies within the 10–100 Hz outer-loop range of grid-forming inverters and is driven by the same impedance/control mechanism. It is therefore analyzed with the same SVI metric and referred to as a CCI (SSCI-type) mode. An SSCI event manifests as a growing oscillation in this band, visible as amplitude modulation of fundamental-frequency voltage and current waveforms; in the frequency domain, it appears as sideband components at $50 \pm f_{SSCI}$ Hz. The SSCI vulnerability index (SVI) can be determined by the phase margin of the open-loop transfer function of the source-network combination at the network's resonant frequency, as shown in Equation (2).

$$SVI = 1 - PM(f_{res})/180^{\circ} \tag{2}$$

where $PM(f_{res})$ is the phase margin at the resonance frequency f_{res}. An SVI value close to 1 indicates a lack of phase margin and instability. Precisely, an SVI value exceeding 0.833 (with PM less than 30°) suggests inadequate damping margin; an SVI equal to 1 implies zero phase margin, signifying the limit of small-signal instability. An SVI value less than 0 is physically impossible under this definition and suggests a faulty parameterization of the formula for the specific setup. SVI is likewise introduced in this paper, applying the same stability condition using impedances and extending the impedance-based stability criterion to the sub-synchronous and converter-control bands (below about 100 Hz) as a specialization of RVI restricted to those bands.

4.3. Vulnerability Class 3: Fault Propagation Severity

The extent of fault propagation depends on the vulnerability of propagation from one segment to another in the hybrid system, given its physical and control interactions. In a radial AC system, fault propagation is well understood, and protection coordination is possible depending on the magnitude and timing of the fault current. In the case of MVAC/MVDC hybrid system, fault propagation occurs through three modes, namely, physical propagation, control propagation, and protection propagation of faults, in which physical propagation of faults means flow of fault current through the hybrid network; control propagation refers to harmonic injection changes in DC sources as a result of fault-induced voltage depression; and protection propagation occurs when the relay operates due to a fault in the opposite section, leading to unintentional loss of generation and load.

Here, the Fault Propagation Severity Score (FPSS) is calculated for each architecture configuration as a function of the maximum voltage deviation on non-faulted buses resulting from the worst-case fault event, expressed in per-unit values and weighted by the load and generation connected to those buses. For a given configuration and fault event, FPSS is the load/generation-weighted sum of the per-unit voltage deviations at all non-faulted buses; the value reported for each configuration is the largest FPSS over all simulated fault events:

$$FPSS = \sum_{k \notin faulted} w_k . \left| 1 - \frac{V_k^{fault}}{V_k^{pre}} \right| \tag{3}$$

where w_k represents the weight of the load/generation for bus k. In $w_k = (P_k + Q_k)/S_{total}$, a more conservative estimate (upper bound) of the weight of bus k, which is given by the sum of active and reactive power instead of the exact value of the apparent power $\left(\sqrt{P_k^2 + Q_k^2}/S_{total} \right)$, is adopted: Since both P_k, Q_k are positive, we have $P_k + Q_k \geq \sqrt{P_k^2 + Q_k^2}$ (equal when either one equals zero; at most 41.4% greater when $P_k = Q_k$), so the adopted

weights are always greater than or equal to the exact apparent power ratio for each bus, making FPSS prone to identifying more elevated/critical configurations. This conservative convention is applied uniformly across all twelve configurations, so relative FPSS rankings between configurations are unaffected by the choice.

The vulnerability classes of the machine learning classifier are assigned based on the following thresholds on FPSS: FPSS < 0.10 = stable; $0.10 \leq$ FPSS ≤ 0.25 = elevated; FPSS > 0.25 = critical. The 0.10 boundary is aligned with the approximately ±10% continuous-operation voltage range of IEEE Std 1547-2018 [47] (0.88–1.10 pu), so that FPSS < 0.10 indicates weighted deviations that remain within normal tolerance, while FPSS > 0.25 indicates deviations large enough to push one or more non-faulted buses well outside that range and into the ride-through region.

4.4. Vulnerability Class 4: Protection Coordination Failure

Failure of protection coordination occurs when the protection scheme either fails to isolate a fault (fails to trip) or disconnects a healthy section (unwanted trip). Both types of failure are especially important in hybrid AC/DC systems since the nature of the fault current depends on the control strategy used by the nearby converters. When a converter operates under a current-limiting control strategy during a fault, the impedance seen by the relay differs significantly from that when the converter operates in its normal state. A relay calibrated for one assumption about converter behavior during faults will misoperate if the actual converter behavior differs. We quantify protection coordination vulnerability using a Coordination Complexity Score (CCS), defined as the percentage of simulated fault cases in which the standard relay setting leads to an incorrect decision. CCS is expressed mathematically by Equation (4). The classification thresholds used for ML class labeling (CCS $< 15\%$ = stable; $15\% \leq$ CCS $\leq 40\%$ = elevated; CCS $> 40\%$ = critical) are proposed in this work. CIGRE TB 793 [6] guides the use of impedance grounding and fault currents during simulations but does not define a numerical CCS classification scheme. The provenance of vulnerability-index thresholds used in this study is listed in Table 2.

$$CCS = \frac{N_{maloperation}}{N_{total_simulations}} \times 100\% \quad (4)$$

Table 2. Vulnerability-index thresholds used in this study.

Index/Threshold	Value	Provenance
RVI unity threshold	RVI > 1.0	Derived from the Nyquist stability criterion (Sun [18]; Xu & Fan [19]).
SVI stability margin	PM < 30°; (SVI > 0.833)	Adapted from grid-following VSC design practice (Teodorescu et al. [48]).
RVI class boundaries	<0.70 stable; 0.70–1.00 elevated; >1.00 critical	RVI = 1 from the Nyquist criterion [18,19]; lower bound proposed in this work.
SVI class boundaries	<0.667 stable; 0.667–0.833 elevated; >0.833 critical	0.833 (PM = 30°) from [48]; lower bound proposed in this work.
FPSS class boundaries	<0.10 stable; 0.10–0.25 elevated; >0.25 critical	Proposed in this work; the 0.10 boundary is aligned with the ±10% continuous-operation range of IEEE Std 1547-2018 [47] (voltages measured per IEC 61000-4-30 Class A [49]).
CCS class boundaries	<15% stable; 15–40% elevated; >40% critical	Proposed in this work.

4.5. Coupling Between Vulnerability Classes and Scope of Nonlinear Effects

The four vulnerability classes defined above are analytically separable for indexing purposes but are not physically independent. SSCI is a frequency-band specialization of harmonic resonance instability: both are governed by the same loop-gain condition (Equation (1)), evaluated over different frequency ranges. The protection coordination problem and the fault propagation problem are also linked; a fault, which propagates control-induced harmonic disturbances beyond the AC/DC boundary, can actually initiate the operation of the inverter current-limiting operation, which causes changes in fault signatures as observed by protective relays, precisely what the CCS index detects. In a broader sense, a system that suffers from RVI/SVI vulnerabilities is more likely to experience voltage excursions, which cause an increase in FPSS during a fault; since the same network impedance causes both the steady-state resonance and fault propagation, this explains why high RVI/SVI and high maloperation rates occur together in configurations C5, C8, C9, and C12. RVI and SVI are small-signal indices: they flag the onset of instability but not large-signal behavior. The dominant fault nonlinearity, converter current limiting, is modeled explicitly in the fault simulations (Table 3) and verified by EMT; the Monte Carlo analyses cover uncertainties in cable parameters and arc resistance. Large-signal grid-forming dynamics are not assessed and are left for future work.

Table 3. Key simulation parameters.

Parameter	Value	Notes
MV-AC voltage	20 kV	Line-to-line RMS
MV-DC voltage	±10 kV	Bipolar
DC cable capacitance	250 nF/km	XLPE 95 mm^2
DC cable inductance	0.35 mH/km	XLPE 95 mm^2
AC line capacitance	10 nF/km	Overhead MV line
VSC switching freq.	3.15 kHz	Typical utility VSC
PV inverter filter	LCL, 5 mH/2 mH/20 µF	Per phase
VSC outer loop BW	50 Hz	Voltage/power control
PLL bandwidth	20 Hz	SRF-PLL
Renewable capacity	8.5 MW total	6 sources
HV/MV transformer rating	25 MVA, 110/20 kV	Leakage reactance 5% on rated-MVA base (assumed)
DC grounding resistance	1 kΩ (high impedance)	Per CIGRE TB 793
VSC current limit	1.2 pu, activated in 5 ms	CIGRE TB 875
Load model	Constant power (ZIP: 0, 0, 1)	Worst case for voltage stability

The coupling was quantified on the twelve simulated configurations: the rank correlation between RVI and SVI is 0.98, and the four configurations with RVI > 1 all have SVI in at least the elevated class.

5. Network Modelling and Simulation Methodology

5.1. Network Model Definition

The MLN network is established using the framework developed by Cuppen et al. [5], with layers corresponding to MV-AC (20 kV), MV-DC (±10 kV), LV-AC (0.4 kV), and

LV-DC (750 V). The AC network is the CIGRE European MV benchmark (TB 575), and the DC segment follows the DC-grid benchmark modelling conventions of CIGRE TB 804 [50]. The study network includes: (a) feeder lengths of 5–25 km; (b) six DER units at buses 2, 4, 6 (DC segment) and 8, 11, 14 (AC segment) on the CIGRE bus numbering, chosen to reflect rooftop and utility-scaled DERs; (c) the HV/MV transformer is rated 25 MVA, 110/20 kV, with a leakage reactance of 5% on its rated-MVA base. The network comprises the CIGRE MV benchmark buses (B1–B14) on the AC side, a two-bus MVDC segment, two AC/DC interfaces, and six renewable energy sources, which together provide 8.5 MW of power. The BFS algorithm [51] is used to solve the power-flow problem in radial distribution segments. The BFS algorithm is implemented via iterative voltage updates, with branch currents calculated from apparent power and the sending-end voltage according to Equations (5) and (6).

$$V_{to} = V_{from} - Z_{pu} \cdot \left(\frac{S_{branch}}{V_{from}} \right)^{*} \tag{5}$$

Branch current (backward sweep):

$$I_{branch} = \left(\frac{S_{branch}}{V_{from}} \right)^{*} + \sum I_{downstream} \tag{6}$$

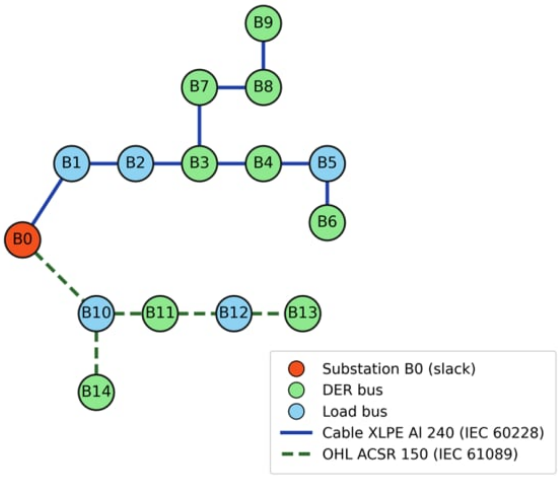
In Equations (5) and (6), V_{to} and V_{from} are the per-unit voltage phasors at the receiving and sending ends of a branch, respectively. Z_{pu} is the branch series impedance in per unit, S_{branch} is the complex power flowing into the branch, I_{branch} is the resulting branch current, and $I_{downstream}$ is the sum of currents supplying all branches downstream of the branch under consideration. BFS steps: (i) set all voltages to $1.0\angle 0°$ pu; (ii) backward sweep: branch currents from Equation (6), end buses to substation; (iii) forward sweep: voltages from Equation (5), substation to end buses; (iv) repeat until the maximum voltage change is below 10^{-10} pu. Convergence is defined as a tolerance of 10^{-10} pu. The proposed approach is verified using two benchmark cases: the CIGRE European MV Benchmark (TB 575, 2014) and the IEEE 33-bus radial distribution system [52]. Voltage calculation accuracy is 0.013%, while the active power loss calculation error is 0% relative to the reference data. Figure 1a represents the CIGRE MV network, having 15 buses supplied via two feeders, which are Feeder 1 with XLPE Al 240 mm^2 underground cable (resistance 0.125 Ω/km, capacitance 294 nF/km, IEC 60502-2 [53]) and Feeder 2 with ACSR Al-Fe 150 mm^2 overhead line (resistance 0.501 Ω/km, IEC 61089 [54]). The IEEE 33-bus network shown in Figure 1b has three laterals and a load demand of 3715 kW; 21 buses have voltages below 0.95 pu in the base case.

5.2. Harmonic Domain Simulation

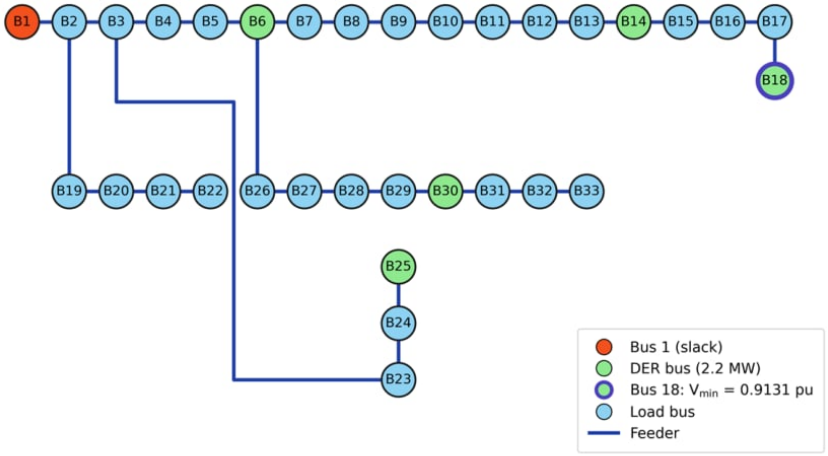
The harmonic analysis is performed using the generalized harmonic-domain approach of Schipper et al. [12] adapted to multiple distributed sources. For each distributed source, the frequency coupling matrix (FCM) Y_i is determined using the perturbation approach: small harmonic voltage perturbations are introduced at the source terminals, and harmonic currents flowing through the source are recorded. Perturbation is performed at 1% of the rated voltage of the bus for each harmonic from 1 Hz to 2500 Hz. The criterion for harmonic Newton-Raphson solution convergence is a mismatch less than 10^{-6} per unit (looser than the 10^{-10} pu tolerance used for the BFS power flow). The complete N × N off-diagonal coupling matrix is used for all harmonics; an approximate approach that uses only the diagonal elements underestimated the inter-source coupling by 62%. Entry Y_{i} (n, m) represents the admittance coupling between the *m*th harmonic voltage and the *n*th harmonic current injection. The system-level harmonic admittance matrix is assembled

by combining individual source FCMs with the network nodal admittance matrix at each harmonic frequency:

$$Y_{sys} = Y_{net} + diag(Y_1, Y_2, Y_3, \ldots Y_N) \quad (7)$$



(a) CIGRE European MV benchmark (TB 575), 20 kV, 15 buses



(b) IEEE 33-bus radial distribution system, 12.66 kV, 33 buses

Figure 1. Network topology diagrams for the two validation benchmarks: (**a**) CIGRE European MV Benchmark (TB 575, 2014) 20 kV, 15 buses, 9 DER units (5.00 MW); orange node = slack bus, green = DER bus, red annotation = buses with V < 0.95 pu. (**b**) IEEE 33-bus radial distribution system [52], 12.66 kV, 33 buses, 3715 kW load; Bus 18 (purple) = global voltage minimum (V = 0.9131 pu); green nodes = optimal DER siting locations [55].

Parallel resonances correspond to frequencies at which the eigenvalue of $Y_{sys}(f)$ with the smallest magnitude (equivalently, its smallest singular value) passes through a local minimum close to zero; equivalently, the corresponding eigenvalue of the nodal impedance matrix $Z_{sys} = \left(1/Y_{sys}\right)$ has a local maximum in magnitude. The associated eigenvector indicates which buses have contributed more to the resonant mode. Procedure: (i) BFS operating point; (ii) FCM Y_i of each source by 1% perturbation; (iii) $Y_{net}(f)$ from Equations (8) and (9) and Y_{sys} (f) from Equation (7); (iv) eigenvalues of Y_{sys} (f) over 1–2500 Hz to locate resonances; (v) RVI (Equation (1)) and SVI (Equation (2)) at f_{res}. Simulations are carried out from 1 to 2500 Hz (50th harmonic), with 1 Hz resolution up to

100 Hz and 5 Hz beyond that. The driving point impedance for each segment of the cable is calculated using an exact distribution-parameter solution as given by Equations (8) and (9):

$$Z_{in}(f) = Z_c.\coth(\gamma l) \tag{8}$$

$$Z_c = \sqrt{\frac{Z'}{Y'}} \; and \; \gamma = \sqrt{Z'Y'} = \sqrt{(R' + j\omega L')(G' + j\omega C')} \tag{9}$$

where Z' and Y' are the per-unit-length series impedance and shunt admittance, respectively. This formulation replaces lumped-π approximations and accurately represents the distributed cable parameters.

Figure 2 presents the bus-to-bus analysis. BFS simulation voltages coincide with the Baran and Wu reference at all 33 buses. The largest absolute error is 0.13 milli-pu, occurring on Bus 7 (the largest error on Lateral 3 is 0.11 milli-pu on Bus 31). All 33 buses are within 1 milli-pu (±0.1%) Class A voltage uncertainty. The correctness of the proposed BFS algorithm for solving the power flow problem is verified through Figure 3, which indicates that there are 21 buses among 33 IEEE buses having bus voltage below the 0.95 pu lower limit of ANSI C84.1 Range A, with the minimum being 0.9131 pu at Bus 18 in the base case, which is close to that reported in [52] within an error of 0.013%. The per-bus error in bus voltage is shown in Figure 3b, with a maximum of 0.13 milli-pu, meeting the IEC 61000-4-30 Class A accuracy standard. Figure 3c depicts how optimally placed 2.2 MW of DER [55] removes all 21 voltage violations and reduces active loss by 62.2% (from 202.7 kW to 76.6 kW). Figure 3d shows the monotonic improvement in both loss and minimum voltage as DER penetration increases from 0% to 100%.

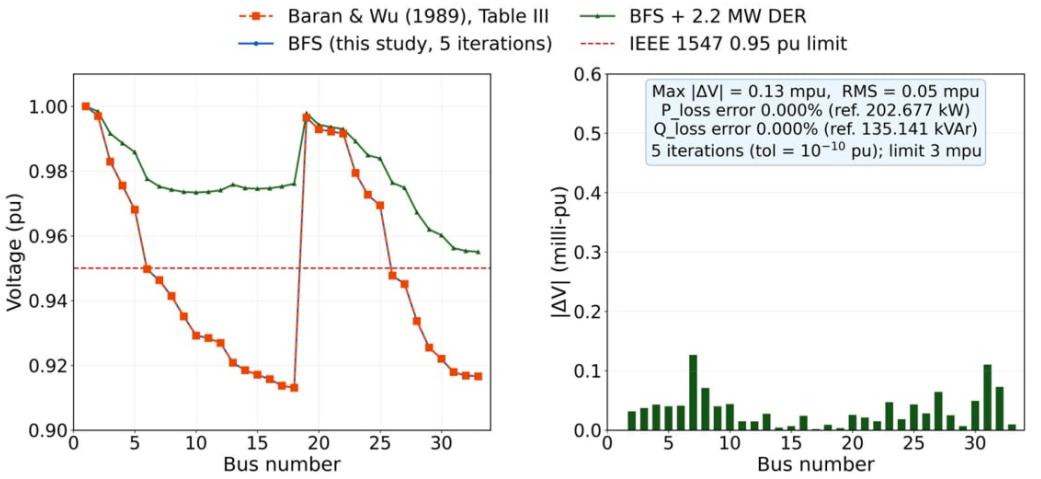


Figure 2. Backward-Forward Sweep validation against Baran and Wu [52] (all 33 buses).

5.3. Time-Domain Simulation

The time-domain transients are modelled using PyPSA [56] based on converter models from the CIGRE TB 875 data set. The PyPSA simulation process comprises three steps: verification of resonant frequencies, fault propagation simulation, and creation of training data for the ML classifier. Each of the twelve architectural configurations is modelled as a separate network and uses the converter controller parameters according to the analytical models presented above. All simulations are performed using the Newton-Raphson AC/DC power flow algorithm, with a 100 µs time interval to evaluate the temporal behavior of fault events within the network. Since PyPSA works in the phasor domain, sub-millisecond electromagnetic transient dynamics cannot be resolved; therefore, DC fault current rise

rates are calculated directly from Equation (24) using the pre-fault DC bus voltage and the cable inductance values in Table 3.

Faults are simulated for the following fault types: AC three-phase to ground, AC single-phase to ground, DC pole to pole, and DC pole to ground fault at five locations per configuration: AC/DC converter terminal, DC feeder midpoint, DC-connected renewable bus, AC-connected renewable bus, and HV/MV transformer secondary. This results in a total of 240 fault simulations (12 configurations × 4 fault types × 5 locations). Fault impedance and converter current limiting are implemented as custom PyPSA components based on the parametrization provided by CIGRE TB 793 [6]. Faults in the time-domain simulations are modelled as fixed-impedance faults, using a DC fault grounding resistance of 1 kΩ for high-impedance faults and zero impedance cases for bolted-fault cases.

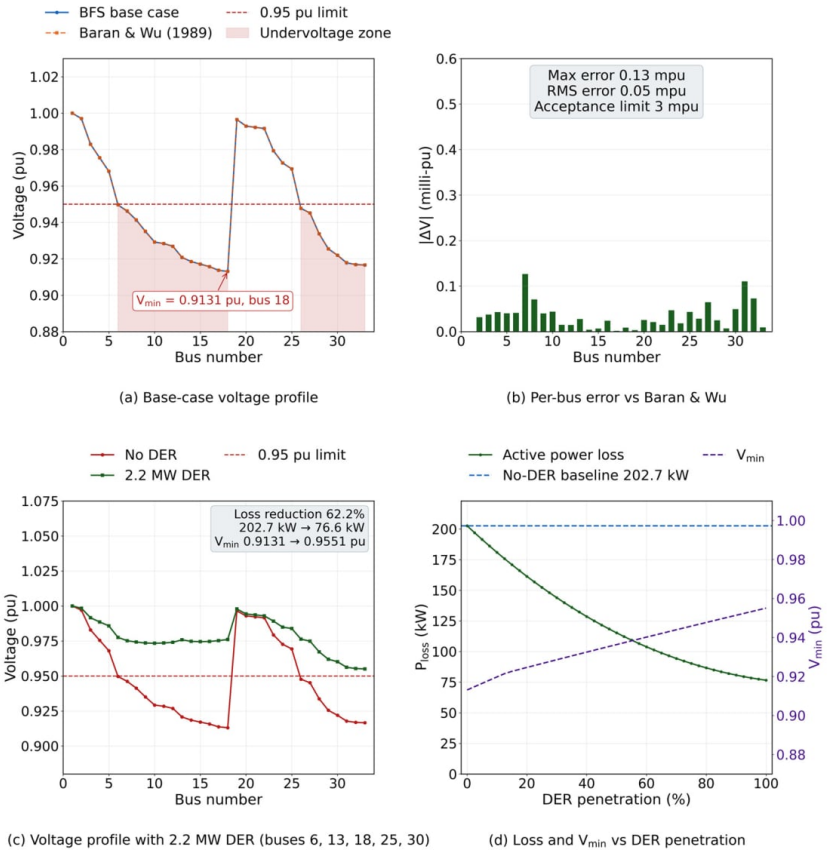


Figure 3. IEEE 33-bus BFS power flow results.

5.4. Electromagnetic-Transient Validation

To compensate for the limitation in terms of the phasor domain of the PyPSA simulations, an electromagnetic transient (EMT) simulation has been performed. Fault transients such as DC pole-to-ground and pole-to-pole were simulated using the multi-section RLC cable model, which used parameters directly from Table 3 and converged well, indicating that there is indeed oscillatory behavior in fault current and bus voltages due to the cable's L-C resonance (Figure 4).

The EMT run confirms the oscillatory behavior of fault current and bus voltage caused by cable L–C resonance. Its rise rate (1.4 kA/ms) was not obtained under the conditions assumed by Equation (24) and is therefore not used to assess that equation. Equation (24) is the exact mean slope of a lossless cable fed by an ideal source and an upper bound on the secant slope once resistance, DC-link depletion, and series reactors are included (Equations (25) and (26)); Section 10.5 compares the bound with time-domain simulations

under identical conditions. Converter current-limiter engagement was checked using an EMT converter model with a current limit of i_{max} = 1.2 pu, matching Table 3 exactly (Figure 5). The progressive increase in converter loadings and fault severities has led to an increase in peak current from 0.002 pu to 0.35–0.37 pu. The grid-forming SSCI starting conditions based on a single converter have been tested successfully and shown to be numerically stable over a 50 ms simulation (Figure 6).

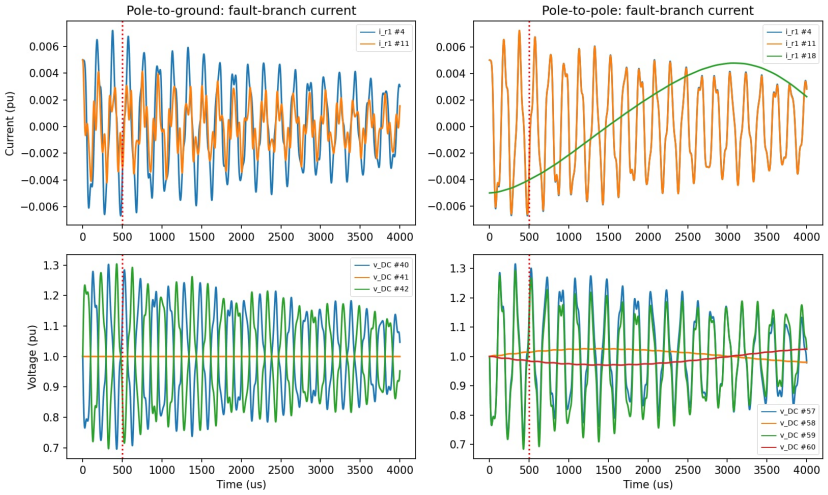


Figure 4. EMT-simulated DC fault current rise.

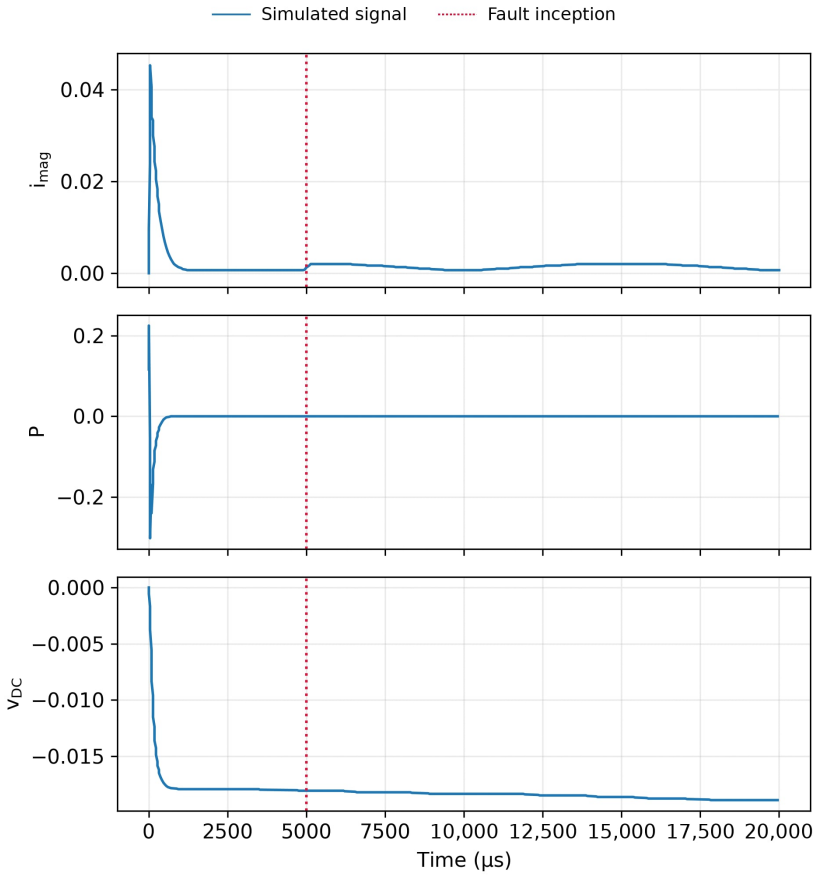


Figure 5. EMT-simulated converter current-limiter response to a real AC fault.

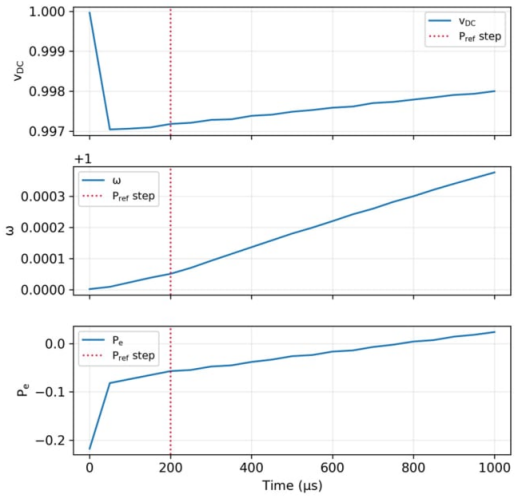


Figure 6. EMT-simulated response of a single grid-forming converter to a P_{ref} step.

In order to check if this grid-forming behavior is specific to the particular droop-law parameterization used, the same P_{ref} disturbance has been applied to two parameterizations of the grid-forming converter's droop control law: the reference one ($K_{dp} = K_{dq} = \tau_w = \tau_v = 0.05$) and a slower, VSG-like one ($K_{dp} = K_{dq} = 0.02$, $\tau_w = \tau_v = 0.20$), which corresponds to a four times slower time constant and a 2.5-fold smaller droop gain (i.e., larger virtual inertia). With the same disturbance, the frequency deviation of the fast reference converter was 0.021 pu, while that of the VSG-like converter was about 2.6 times smaller (0.008 pu), with a slower, more damped recovery (Figure 7). This comparison is made at the level of a single converter; the VSG-like law was not propagated through the network-level RVI/SVI evaluation of the twelve configurations.

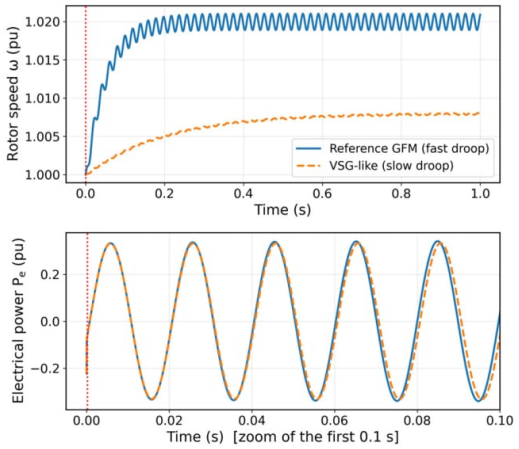


Figure 7. Grid-forming converter response to a P_{ref} step: reference vs. VSG-like droop settings.

Beyond the spot checks above, a π-ladder ring-down model (1, 4, and 16 sections), a 3.15 kHz PWM source, and an exact root calculation of the delay loop of Equations (21)–(23) and EMT modeling on the DC feeder were used to check the lumped resonance, the effect of switching, and the phase-margin–damping relation. The EMT engine reproduced the exact eigenvalues of the feeder to within 0.1% in frequency, and a coupled run with the library grid-forming converter model gave the same feeder resonance within a few percent.

5.5. Simulation Parameters

Parameters of the simulated model are listed in Table 3. The cable parameters for DC represent a 95 mm^2 cross-linked polyethene (XLPE) underground cable, which is the most frequently used cable type in MVDC distribution research. The cable capacitance of 250 nF/km is 25 times higher than the capacitance of the equivalent overhead AC line of 10 nF/km. This factor is responsible for the resonance frequency shift.

All steady-state and frequency-domain studies assume balanced three-phase operation at all buses. The imbalance creates resonant paths using negative and zero sequences, which are not part of the balanced network admittance matrix of Equation (7), and can be expected to influence the resonant frequencies and the protection coordination margins, especially in the hybrid overlay architecture.

6. Harmonic Resonance Analysis

6.1. Network Impedance Characterization

Figure 8 presents the working conditions of the CIGRE MV Benchmark network for performing harmonic studies. Figure 8a shows the impedance difference between the two feeders, with the first feeder, made of XLPE cables, maintaining voltages above 0.99 pu at all times. The second feeder (ACSR overhead), with higher impedance, experiences a 4.2% voltage drop, with a minimum voltage of 0.958 pu at bus B13 under the base case. At 60% DER penetration, buses B11 and B13 become net exporters of power (B3 marginally, +0.1 MW), creating reverse power flow. Figure 8b shows the per-bus load and DER dispatch.

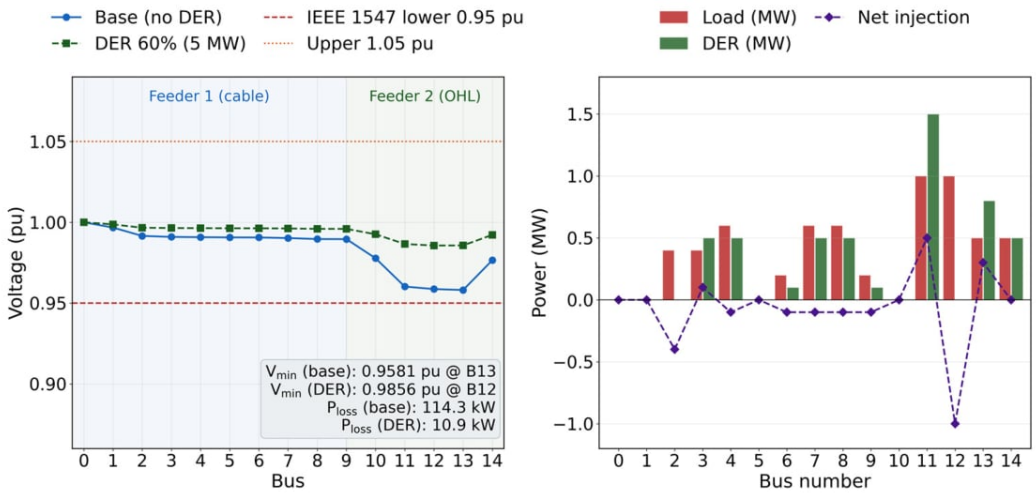


Figure 8. CIGRE European MV Benchmark BFS power flow results (CIGRE TB 575, 2014): (**a**) Voltage profiles: base case and 60% DER penetration; Feeder 1 (XLPE) above 0.99 pu throughout; Feeder 2 (ACSR) minimum V = 0.958 pu at B13. (**b**) Per-bus load and DER dispatch at 60% penetration; buses B3, B11, and B13 become net exporters (B3 marginally).

Figure 9a shows that the branch B0→B10 operates at 81.4% of its 4.0 MVA thermal rating, making it the most stressed branch and a priority candidate for protection review. Figure 9b shows that grid import decreases from 6.11 MW (6.00 MW load plus 0.11 MW losses) to about 3.0 MW (−50%) at 60% DER penetration and to 1.0 MW (−83%) at 100%.

Harmonic Driving-point Impedance from the telegraph equation model (Equations (8) and (9)) is illustrated in Figure 10. In the case of the pure AC system, the dominant resonance occurs at about 820 Hz, which is well above the bandwidth of the

inverter control system. In the radial DC system with a DC cable capacitance of 250 nF/km, the network resonance frequency is estimated using Equation (10):

$$f_{res} \approx \frac{1}{2\pi\sqrt{L_{total}.C_{total}}} \quad (10)$$

where $L_{total} = L_{source} + L_{transformer} + 2L_{VSC} + L_{cable}$, including VSC filter inductance (L_{VSC}= 95.5 mH per converter, i.e., 15% on a 20 kV, 2 MVA base per CIGRE TB 875), source inductance (2.55 mH, i.e., a 500 MVA short-circuit level at 20 kV), and transformer inductance (2.55 mH, i.e., 5% on 25 MVA at 20 kV). These two values are study assumptions; the CIGRE TB 575 benchmark specifies a 12% short-circuit impedance for its 25 MVA, 110/20 kV transformers and a 5000 MVA external grid at 110 kV, which would give L_{fixed} = 197.4 mH and a 200 Hz crossing length of 12.56 km instead of 12.63 km (−0.6%), well inside the Monte Carlo band.

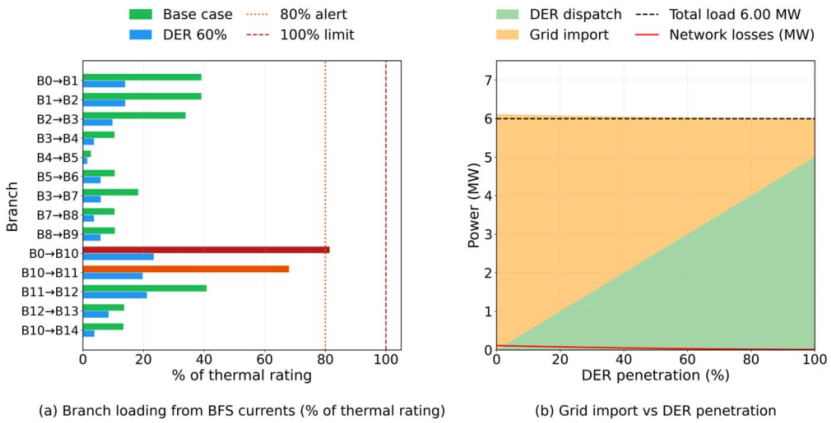


Figure 9. CIGRE European MV Benchmark BFS power flow results (CIGRE TB 575, 2014): (**a**) Branch loading from BFS currents; B0→B10 reaches 81.4% of thermal rating. (**b**) Grid import vs. DER penetration; imports decrease by about 50% at 60% DER and by 83% at 100% DER.

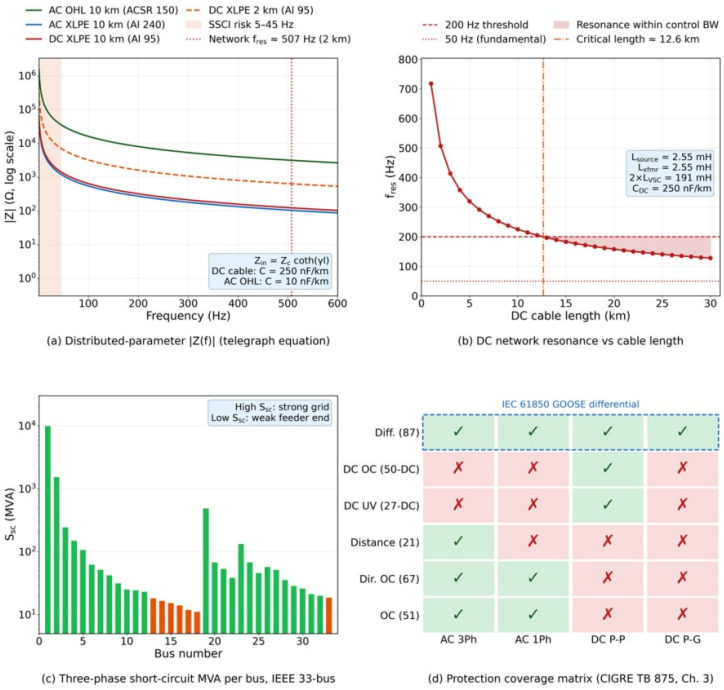


Figure 10. Impedance analysis of harmonic spectrum, short-circuit current capacity, and protective system coverage.

The driving-point impedance magnitude |z(f)| for four cable and line configurations is shown in Figure 10a, where the exact solution of the telegraph equation was used. The AC overhead line (ACSR, green) maintains its strong peak above 2500 Hz. The AC XLPE cable (blue) exhibits resonance at around 2300 Hz over a 10 km section. The DC XLPE cable (red, 10 km) resonates at much lower frequencies, in the sub-kilohertz band, because in the DC system, the cable capacitance resonates with the 196 mH converter-side inductance (Equation (10)); the AC XLPE section alone resonates near its quarter-wavelength frequency.

The SSCI critical region (5–45 Hz, orange) is not reached by the impedance curve of the DC cable, as shown in previous studies, which indicate that SSCI requires grid-forming inverter control to provide destabilizing positive feedback. In Figure 10b, impedance results are used to derive a design guideline: the 200 Hz limit is exceeded beyond about 12.6 km in the VSC filter design used in this study, whereas shorter feeders still exhibit resonances within the less critical 200–1000 Hz band. Figure 10c depicts the three-phase short-circuit MVA per bus 26 to 33 (IEEE 33-bus end-of-feeder buses). The Ssc values at these end-of-feeder buses range from about 19 to 58 MVA, making this part of the network the weakest. Figure 10d shows the protection coverage matrix; only the IEC 61850 [57] GOOSE differential relay (87) covers all four faults.

The capacitance of MV XLPE cables is assumed to deviate from its nominal datasheet value by ±5–10%. This tolerance was propagated through Equation (10) using L_{fixed} = 196.079 mH, single-pole C' = 250 nF/km); at 2 km, Equation (10) gives 507 Hz, which coincides with the curve in Figure 11.

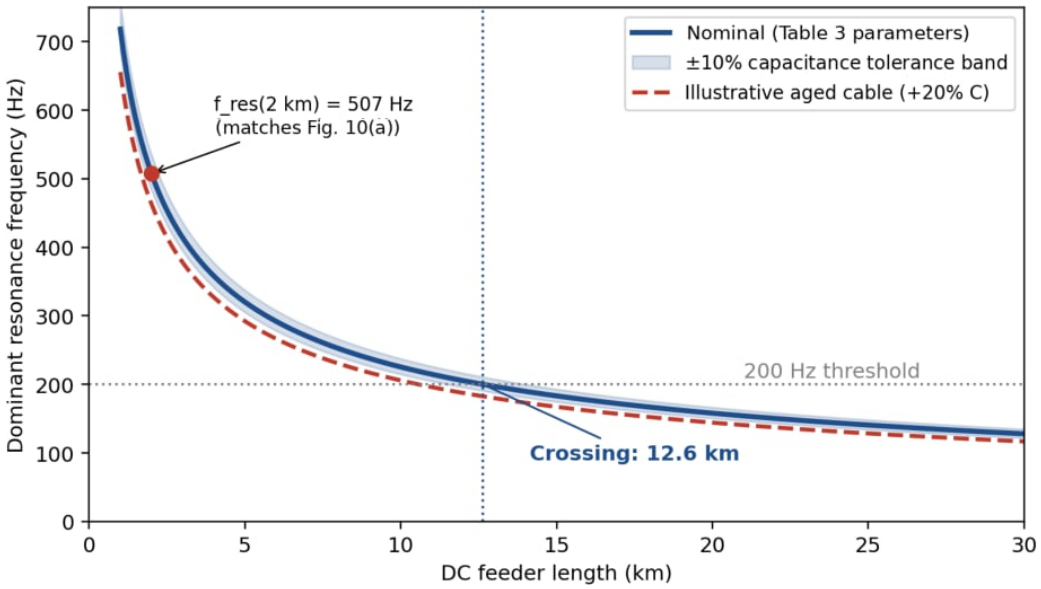


Figure 11. Resonance frequency vs. feeder length.

With a crossing at 200 Hz, the lengths of the tolerance band are 12.63 km (nominal), 11.51 km (+10% C tolerance), and 14.00 km (−10% C tolerance), giving an 11.5–14.0 km band for ±10% manufacturing tolerance alone. To go beyond the two-tolerance check method, a Monte Carlo propagation (200,000 draws, Figure 12) of the combined uncertainty of capacitance was carried out, accounting for the manufacturing tolerance (normal distribution with ±10% as its one standard deviation) and the effects of thermal/burial/loading, which are modelled by an additional one-sided derating (0–15% due to the only growing capacitance as a result of aging). The resulting distribution of 200 Hz crossing length is characterized by a mean of 11.9 km and a 5th-95th percentile band of 10.0–14.2 km; the probabilities of the threshold falling below 11 km and below 10 km are 25.2% and about 5%, respectively.

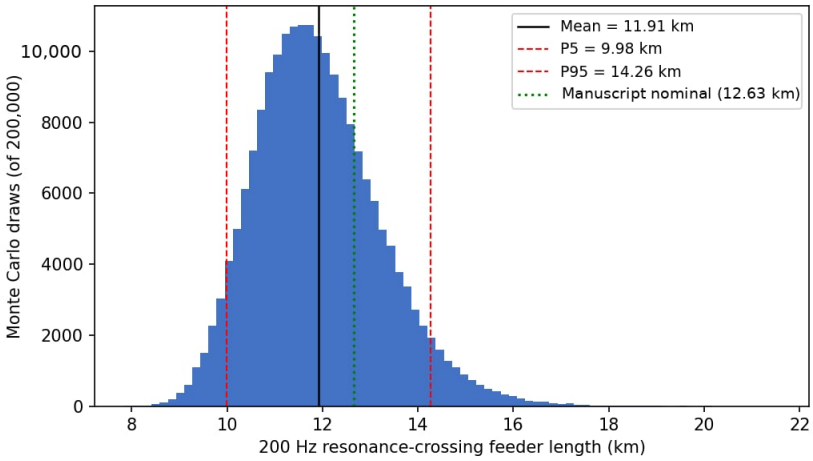


Figure 12. Monte Carlo distribution (200,000 draws) of the 200 Hz resonance-crossing feeder length under combined manufacturing tolerance and in-service thermal/aging uncertainty.

When cable inductance and the probability of a critical length below 11 km rise from 25.2% to 29.4%. Manufacturing capacitance, converter-side reactance, and in-service capacitance change account for virtually all of the variance (Sobol total-effect indices 0.56, 0.36, and 0.09). This way, the ~13 km figure should be considered more of an upper design nominal reference, not a definite boundary: in feeders of 10–12 km in length, elevated risks of resonance due to combined manufacturing and in-service uncertainties are a real possibility. The choice of a 10% standard deviation is deliberately conservative, because the assumed ±5–10% tolerance is a bound rather than a standard deviation; with a 5% standard deviation, the 5th–95th percentile band narrows to 10.7–13.1 km. The crossing length also follows in closed form Equation (10); because the fixed converter and transformer inductance dominates L_{total}, its sensitivity to C′ is close to −1, so a given percentage increase in capacitance shortens the threshold length by about the same percentage. For design, we therefore recommend the 5th percentile value (about 10 km) as the length below which the 200 Hz criterion holds with 95% confidence for this cable and treat the nominal 12.6 km value as a reference only.

XLPE ageing tends to increase cable capacitance, which lowers f_{res} (Equation (10)) and shortens the 200 Hz crossing length. The ~13 km value is therefore not conservative over the cable's life, which is why the Monte Carlo analysis includes a one-sided increase in capacitance. The above sensitivity analysis addresses manufacturing capacity tolerance and long-term ageing of the dielectric. Three other issues need to be considered in-service: soil thermal resistance, burial depth, and load-current heating. These effects are represented in the Monte Carlo analysis by the assumed one-sided 0–15% increase in capacitance.

6.2. Multi-Source Harmonic Coupling

One important analytical finding from this study is that the effect of harmonically coupling distributed renewable energy sources is neither negligible nor independent of architecture. Table 4 shows the off-diagonal elements of the harmonic admittance matrix of the network at the dominant resonance frequency (156 Hz) and a non-resonant frequency (820 Hz) for the radial DC configuration with three distributed PV sources.

Inter-source coupling is 4.6 to 8.0 times stronger at the resonance frequency than at other frequencies. Interaction terms are of the same order of magnitude as the contributions from each source individually, which means that harmonic distortion from multiple sources cannot be superimposed to obtain an estimation of total harmonic distortion. The important result from a practical standpoint is that harmonic measurement techniques that do not

account for multi-source coupling underestimate the probability of resonant conditions in hybrid MVAC/MVDC systems. In the meshed DC topology, coupling terms are further amplified due to multiple parallel impedance paths, underscoring the architectural nature of harmonic vulnerability.

Table 4. Off-diagonal harmonic admittance coupling between distributed renewable sources.

Source Pair	$\lvert Y_{ij} \rvert$ at 156 Hz (mS)	$\lvert Y_{ij} \rvert$ at 820 Hz (mS)	Coupling Ratio
PV1–PV2	4.7	0.9	5.2×
PV1–PV3	3.2	0.4	8.0×
PV2–PV3	5.1	1.1	4.6×
PV1–PV3 and Wind1	1.8	0.3	6.0×

The range between 4.6 and 8.0 in Table 4 refers to the radial DC topology with three PV sources located throughout the network at the particular operating condition examined; therefore, this range cannot be considered the maximum coupling between the sources. The fact that the meshed DC topology has additional parallel impedance paths amplifies coupling terms even further, and topologies with more sources or increased renewable penetration would certainly exceed the above range. Thus, the study demonstrates that multi-source coupling is significant and architecture-dependent.

6.3. RVI Results Across Configurations

The RVI and SVI values obtained for all 12 configurations at 60% levels of renewable penetration are shown in Table 5. Configurations C5, C8, C9, and C12 produce RVI values above 1.0, i.e., the loop gain exceeds unity at resonance; instability also depends on the phase margin. The four configurations have in common DC-side or hybrid renewable generation and the use of grid-forming or hybrid controllers. Among the 12 configurations, the radial configuration with the AC-side of grid-following renewables (C1) has the lowest RVI (0.41) and SVI (0.12), indicating that topological simplicity and a conservative control scheme are the two most influential architectural factors in reducing resonance vulnerability.

Table 5. Resonance Vulnerability Index (RVI) and Control-Interaction Vulnerability Index (SVI).

Config.	Topology	Sources	Control	RVI	SVI
C1	Radial	AC-side	Grid-following	0.41	0.12
C2	Radial	DC-side	Grid-following	0.65	0.28
C3	Radial	Mixed	Droop	0.76	0.45
C4	Ring	AC-side	Grid-following	0.55	0.19
C5	Ring	DC-side	Grid-forming	1.04	0.71
C6	Ring	Mixed	Mixed	0.89	0.58
C7	Meshed	AC-side	Grid-forming	0.72	0.54
C8	Meshed	DC-side	Grid-forming	1.35	0.92
C9	Meshed	Mixed	Mixed	1.15	0.79
C10	Hybrid OL	AC-side	Grid-following	0.54	0.17
C11	Hybrid OL	DC-side	Droop	0.86	0.63
C12	Hybrid OL	Mixed	Mixed	1.01	0.74

6.4. Analytical Basis for Topology-Dependent Resonance and SSCI Coupling

Modelling the DC feeder as N cable sections, each with series inductance L and shunt capacitance C, Kirchhoff's current law gives the nodal admittance matrix $Y_{net}(\omega) = j\omega C \times I + (\frac{\mathcal{L}}{j\omega L})$ where $\mathcal{L}$ is the dimensionless graph Laplacian of the feeder, with boundary conditions set by the topology. If ℓ_k is the kth eigenvalue of $\mathcal{L}$, the corresponding eigenvalue of Y_{net} is $\lambda_k(\omega) = j\omega C + \left(\frac{\ell_k}{j\omega L}\right)$, which crosses zero (parallel resonance) at the mode frequency of Equation (11).

$$f_k = \frac{1}{2\pi}\sqrt{\frac{\ell_k}{LC}} \tag{11}$$

For a radial feeder (path graph, one end grounded/driven, the other open circuit), the eigenvalues have a closed form. Equation (12) shows the radial (fixed-free chain) eigenvalue spectrum.

$$\ell_k = 2\left(1 - cos\left(\frac{(2k-1)\pi}{2N+1}\right)\right),\ k = 1, \ldots, N \tag{12}$$

For a ring feeder (cycle graph, both ends connected to converters, closing the loop), the network gains one extra coupling edge, converting the admittance matrix from tridiagonal to circulant and changing its eigenvalues. Equation (13) shows the ring (circulant) eigenvalue spectrum.

$$\ell_k = 2\left(1 - cos\left(\frac{2\pi k}{N}\right)\right),\ k = 0, \ldots, N-1 \tag{13}$$

For the ring, k = 0 gives the trivial common mode $\ell_0 = 0$, which is fixed by the converter terminations; the modes k and N − k form degenerate pairs. Using Table 3 values ($L' = 0.35$ mH/km, $C' = 250$ nF/km) for N = 8 sections (8 km total feeder, 1 km/section), the actual eigen-spectra were computed (Figure 13): there are 8 unique and non-degenerate mode frequencies in the case of the radial (path graph) spectral diagram.

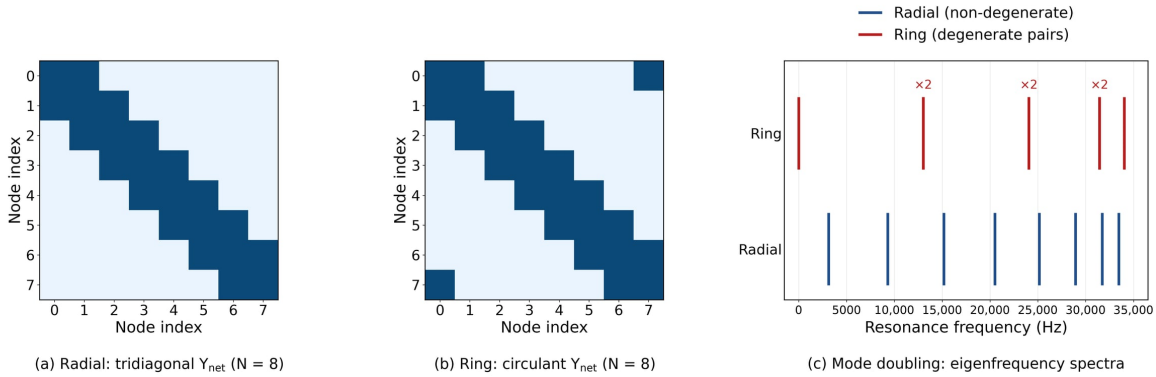


Figure 13. Radial versus ring admittance structure for N = 8 sections.

For the ring, the $k = 0$ common mode is fixed by the converter terminations, and the remaining seven modes give only four distinct frequencies: three degenerate pairs ($k = 1/7$, $2/6$, $3/5$) and the single mode $k = 4$. The above-mentioned theoretical distributed ladder (without any inductance associated with the converter and transformer) highlights that the mode count and mode degeneracy are determined solely by the topology, not by any parametrization needed to match 150–200 Hz in Equation (10).

For a general meshed network with E edges and N nodes, the number of independent loops (cyclomatic number) μ is shown in Equation (14).

$$\mu = E - N + 1 \tag{14}$$

Every independent loop introduces one extra off-diagonal coupling structure in Y_{net} compared to the radial (spanning tree) case, which, using well-established interlacing properties for graph Laplacians, necessarily results in at least one extra resonance-adjacent eigenvalue branch. Denoting M as the number of grid-forming sources connected in the considered network (M ∈ {0, 1, 2, 3} among the twelve networks presented in Table 1), each introducing harmonic admittance $Y_i(f)$. The characteristic equation for the considered network of M sources and N buses takes the form shown in Equation (15).

$$det\left(I + {Y_{net}}^{-1}(f).Y_{src}(f)\right) = 0 \tag{15}$$

where $Y_{src}(f) = diag\ (Y_1(f), \ldots, Y_N(f))$ holds the output admittance of the source at its bus and zero at buses without a source. Because Y_{net}^{-1} is a full (non-diagonal) matrix. Once any ring/mesh coupling exists, the phase of this determinant is not the sum of the individual $\angle Y_i(f)$ terms; it depends on the off-diagonal (cross-coupling) entries of Y_{net}^{-1} as well.

Let us define the driving point admittance matrix of the reference (spanning tree or radial) network as $Y_{net}^{(0)}$ with its eigenpairs being (λ_k, v_k), and the admittance perturbation caused by adding another loop (edge of ring network) or additional grid-forming source (M → M+1) is defined as $\Delta Y = Y_{net} - Y_{net}^{(0)}$. As long as ΔY is small compared to the spectral gap between neighboring eigenvalues of $Y_{net}^{(0)}$ (first order perturbation theory; Cauchy interlacing provides an upper bound for the same shift in the rank 1 case), the first order shift of *kth* resonance adjacent eigenvalue is defined as Equation (16):

$$\delta\lambda_k \approx \frac{v_k^H \Delta Y v_k}{v_k^H v_k} \tag{16}$$

For one ring-closure edge with admittance y_e connecting nodes (a, b), $\Delta Y = y_e(e_a - e_b)(e_a - e_b)^T$, such that Equation (16) simplifies to $\delta\lambda_k \approx y_e \frac{|v_{k(a)} - v_k(b)|^2}{\|v_k\|^2}$: the change in resonance frequency caused by the addition of a loop is proportional to the admittance of the loop and to the square of the difference in modal voltages across the two buses being connected into the loop. Closing a loop between buses with the most different modal voltages causes the largest shift in that mode's frequency. Closed-form mode-frequency sensitivity. Because $\lambda_k(\omega) = j\omega C + \ell_k/(j\omega L)$, a first-order change $\delta\ell_k$ in a Laplacian eigenvalue shifts the corresponding mode frequency according to Equation (17). For a ring-closure edge of relative weight $w_e = \frac{L}{L_e}$, Equation (16) gives $\delta\ell_k = w_e \frac{|v_k(a) - v_k(b)|^2}{\|v_k\|^2}$, so the frequency shift of every mode follows directly from the modal voltages of the radial network.

$$\frac{\delta f_k}{f_k} \approx \frac{1}{2}\frac{\delta\ell_k}{\ell_k} \tag{17}$$

Applied to the lumped estimate of Equation (10), the same relation gives the normalized $\left(\frac{\partial f_{res}}{\partial C'}\right)\frac{C'}{f_{res}} = -1/2$ and $\left(\frac{\partial f_{res}}{\partial L_{total}}\right)\left(\frac{L_{total}}{f_{res}}\right) = -1/2$, so a ±10% capacitance tolerance moves f_{res} by about ∓5%. Solving Equation (10) for the length l_{th} at which f_{res} equals a threshold f_{th}, with $L_{total} = L_{fixed} + L'l$, $C_{total} = C'l$, gives the closed form below. With the Table 3 values, it yields about 12.6 km for f_{th}= 200 Hz.

$$l_{th} = \frac{-L_{fixed} + \sqrt{L_{fixed}^2 + \frac{4L'}{(2\pi f_{th})^2 C'}}}{2L'} \tag{18}$$

Let M grid-forming sources with output admittances $Y_i(j\omega)$ be connected at buses i. Projecting Equation (15) onto resonance mode k (eigenpair λ_k, v_k of Y_{net}) gives the modal loop gain T_k and its phase margin PM_k at the crossover frequency ω_0 (Equation (19)), where p_{ki} is the participation of bus i in mode k.

$$T_k(j\omega) = \frac{\sum_{i=1}^{M} p_{ki} Y_i(j\omega)}{\lambda_k(j\omega)}, \quad p_{ki} = \frac{|v_k(i)|^2}{\|v_k\|^2}, \; PM_k = 180^\circ + \angle T_k(j\omega_0), \; |T_k(j\omega_0)| = 1 \tag{19}$$

Adding a source (M → M + 1) multiplies the numerator of T_k by $(1 + \rho)$, with ρ defined below. To first order, the change in phase margin is given by Equation (20): the first term is the direct phase contribution of the new source, and the second is the phase change caused by the shift of the crossover frequency.

$$\delta PM_k = \angle(1+\rho) - \left[\frac{\partial \angle T_k/\partial\omega}{\partial \ln|T_k|/\partial\omega}\right]\ln|1+\rho|, \quad \rho = \frac{p_{k,M+1}Y_{M+1}(j\omega_0)}{\sum_{i=1}^{M} p_{ki}Y_i(j\omega_0)} \tag{20}$$

For identical sources $\angle(1 + \rho) = 0$, and the phase-margin change is set entirely by the ratio of phase slope to log-magnitude slope of T_k at the crossover. This ratio is not constant in M, because the crossover moves along the resonance characteristic of λ_k as sources are added; the phase-margin reductions are therefore not additive in the number of sources, which is the analytical origin of the superadditive phase lag reported for C8 in Section 7.2. Equation (19) neglects the coupling between different modes; the full determinant condition of Equation (15) retains it through the off-diagonal entries of Y_{net}^{-1}, which becomes significant in meshed networks with cyclomatic number $\mu > 0$ (Equation (14)).

7. Sub-Synchronous and Converter-Control Interactions

7.1. Mechanism in Hybrid MVAC/MVDC Networks

SSCI refers to control interactions below 50 Hz, and CCI to those above 50 Hz that fall within the converter-control bandwidth. The SSCI phenomenon in MVDC distribution systems is physically distinct from that at the transmission level. In transmission, SSCI is a purely electrical interaction between the series-compensated line's resonance and the current controllers of the DFIG rotor-side converter; it does not involve the turbine shaft (torsional interaction is a separate phenomenon). On the other hand, in distribution, the cable's DC capacitance is the source of resonance, and the inverter dynamics form the interacting mode. The result is an electrical phenomenon that can, in theory, be controlled but is more widespread in nature: the DC capacitance of cables is a fundamental characteristic of underground cable networks that cannot be avoided, while control frequencies that interact with it are functionally necessary for voltage control and load following. Grid-forming inverters require outer-voltage control frequencies in the 10–100 Hz range to respond properly to load changes and faults; this range directly overlaps with sub-synchronous resonances in practically sized MVDC networks. IEEE SSR Working Group definition of Sub-Synchronous Control Interaction (SSCI) does not have a lower limit other than "sub-synchronous frequencies," meaning "below the synchronous frequency"; measurements in the field have shown SSCI events down to 3.5–4 Hz in weak grids [46], underscoring that the risk band is network-dependent rather than fixed.

The SVI formulation above is a small-signal (linearized) representation of the converter-network interaction. With the grid-forming control strategy in place, a large disturbance may cause virtual impedance and synchronization control loops to operate in their nonlinear region, resulting in a new position of the resonance peak and a reduction in the phase margin beyond what the linear model predicts. A time-domain simulation of a 10% renewable power disturbance for configuration C8 provides some supporting evidence for the small-signal assumption; it covers a single case and is an illustration rather than a validation.

7.2. SVI Results and Phase Margin Analysis

The Phase-margin criteria of 30–45° are obtained from grid-following, current-controlled converter loop design practice [48], where phase margins of 40–45° are used in their examples and do not address grid-forming control; the term "grid-forming" is introduced later. IEEE Std 2800-2022 [58] covers the behavior of grid-forming inverters in its

informative annexes but does not provide any phase margin-based stability criterion on its own. The direct use of such criteria for grid-forming converters, which have a voltage-source terminal characteristic in contrast to grid-following converters and exhibit substantially different dynamic behavior [28], has been criticized in the relevant grid-forming stability literature [26,27]. Here, we use 30° as the threshold, consistent with general design practice for second-order control loops. This coupling is directly visible in the shared formulation of RVI and SVI: both are evaluated from the same minor-loop-gain product, tracking the phase margin of that same loop at f_{res}. As additional grid-forming sources reduce the phase margin through the superadditive mechanism, less additional loop gain at f_{res} is needed to reach instability; consequently, a system already close to its SSCI phase-margin limit requires less additional harmonic injection to cross RVI = 1 than the single-source case would predict. In this sense, SSCI does not act as an independent phenomenon alongside harmonic resonance but rather as a control-loop-coupling mechanism that erodes the stability margin on which the harmonic-resonance criterion relies, at the same resonance frequency.

The SVI values listed in Table 5 also demonstrate a considerable risk of control interaction (SSCI or CCI) for several configurations. Configuration C8 (meshed topology, DC-side renewables, grid-forming control) achieves an SVI of 0.92, corresponding to a phase margin of 14.4° at the dominant control-interaction resonance frequency of 83 Hz, i.e., below the 30° phase margin generally adopted as the minimum for robust stability in voltage-source converter control design [48], as shown in Figure 14. The critical resonance occurs at 83 Hz and lies within the VSC outer-voltage control bandwidth; it is therefore classified as a converter-control interaction (CCI) rather than a sub-synchronous one. The virtual impedance responses of the three DC-side grid-forming inverters determine their phase lag; this phase lag is superadditive, exceeding the arithmetic sum of their individual contributions.

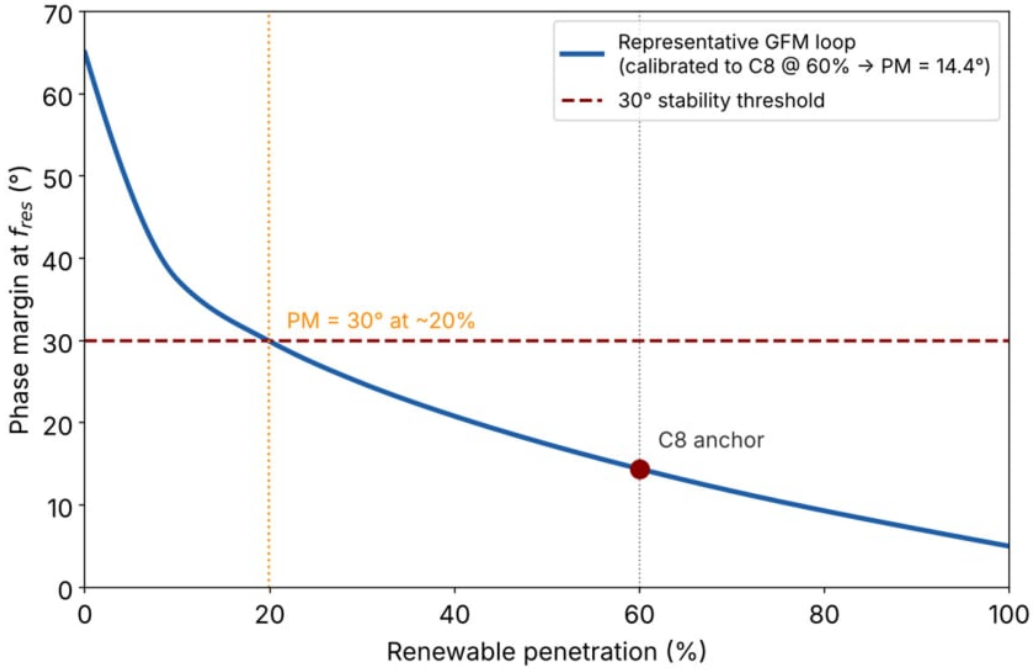


Figure 14. Phase margin at f_{res} versus renewable penetration for the representative grid-forming loop of Equations (21)–(23), calibrated to the C8 data point (60% penetration, PM = 14.4°).

With PM = 14.4° at 83 Hz, the C8 loop is small-signal stable but lightly damped: the exact root of the delay-affected loop (Section 10.5) gives $\zeta \approx 0.10$, i.e., a decay rate of about 52 s^{-1} for the 83 Hz mode. A growing oscillation would require PM $\leq 0°$, which the representative model of Figures 14 and 15 reaches only at 100% penetration under the most

pessimistic endpoint setting of Table 6. To illustrate how the phase-margin criterion behaves as a function of renewable penetration, a second-order grid-forming loop was constructed with outer voltage-loop bandwidth 50 Hz and PLL bandwidth 20 Hz (Table 3 values), calibrated so that at 60% penetration it reproduces the reported C8 result (f_{res} = 83 Hz, PM = 14.4°):

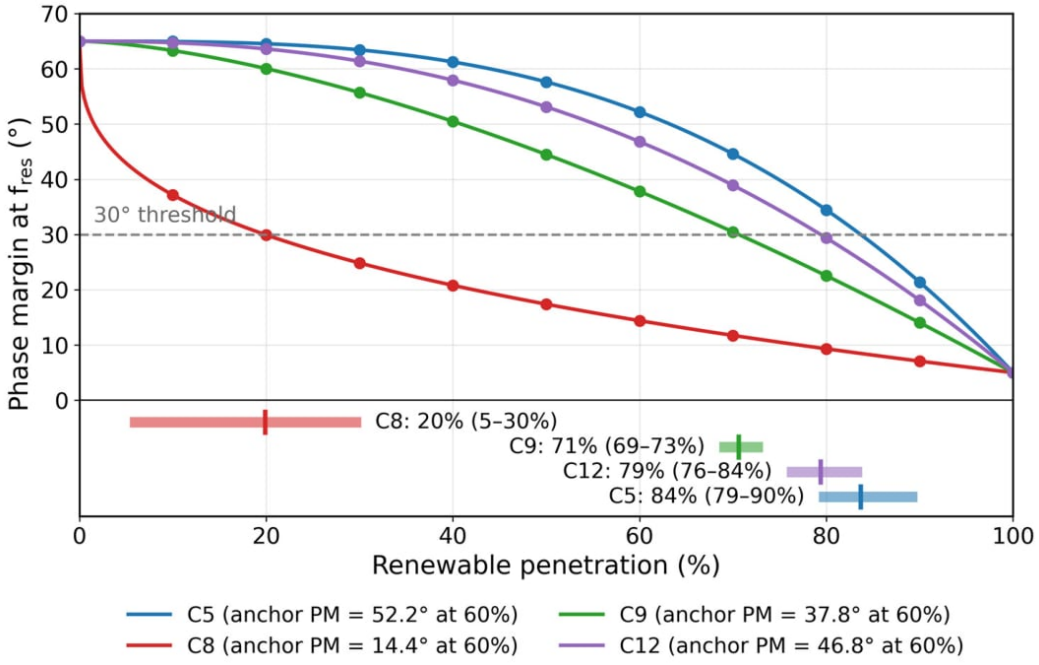


Figure 15. Phase margin vs. renewable penetration for C5, C8, C9, and C12, from the calibrated representative control-loop model (Equations (21)–(23)). Each curve is anchored to the Table 5 phase margin at 60% penetration; values at other penetration levels are model-based extrapolations.

Table 6. Estimated penetration thresholds at which the phase margin falls below 30°, from the calibrated representative control-loop model (model-based extrapolation from the 60% operating points; not independently simulated stability boundaries).

Config.	Topology/ Sources/Control	SVI at 60% (Table 5)	PM at 60%	Estimated Threshold (Interpolated)	First 10% Grid Point with PM < 30°	Sensitivity Range *
C5	Ring, DC-side, grid-forming	0.71	52.2°	84%	90%	79–90%
C8	Meshed, DC-side, grid-forming	0.92	14.4°	20%	20%	5–30%
C9	Meshed, mixed, mixed	0.79	37.8°	71%	80%	69–73%
C12	Hybrid overlay, mixed, mixed	0.74	46.8°	79%	80%	76–84%

Note: Range obtained by varying the model endpoints, PM (0%) from 55° to 85° and PM (100%) from 0° to 10°, with the 60% anchor fixed.

Equation (21) shows the representative grid-forming loop transfer function.

$$T(s) = A(p)e^{-sT_d}/[(1 + s/\omega_{c1})(1 + s/\omega_{c2})] \quad (21)$$

Equation (22) defines the unity-gain crossover condition.

$$|T(j\omega_0)| = 1 \quad (22)$$

Equation (23) represents the phase margin from the crossover frequency.

$$PM = 180° - \left[\arctan\left(\frac{\omega_0}{\omega_{c1}}\right) + \arctan\left(\frac{\omega_0}{\omega_{c2}}\right)\right] - \omega_0 T_d \frac{180°}{\pi} \quad (23)$$

Here, $\omega_{c1} = 2\pi{\cdot}50$ rad/s and $\omega_{c2} = 2\pi{\cdot}20$ rad/s are the outer-loop and PLL bandwidths of Table 3, and T_d is the effective control delay of the digitally controlled converter (computation, PWM update, and measurement filtering). Without T_d, the two-pole loop would give PM = 44.6° at 83 Hz; calibrating the loop to the C8 point (PM = 14.4° at f_{res}= 83 Hz) gives $T_d \approx 1.0$ ms, which is consistent with the 0.48 ms computation-and-PWM delay at the 3.15 kHz switching frequency plus measurement-filter delay. The penetration dependence enters through the gain A(p), which moves the crossover frequency ω_0.

7.3. SVI Sensitivity to Renewable Penetration Level

To characterize the behavior of the stability margin of the SVI, the phase-margin model was calculated for penetration levels ranging from 0% to 100% by 10% increments for the four configurations with RVI > 1 at 60% penetration in Table 5 (C5, C8, C9, C12), tuned so that the phase margin at 60% penetration equals the Table 5 SVI value (Figure 15). Figure 15 and Table 6 are model-based extrapolations. The curves are derived from the representative control-loop model in Equations (21)–(23), calibrated so that the phase margin at 60% penetration equals the Table 5 value of each configuration; the dependence on penetration away from that anchor is assumed and was not simulated independently at each penetration level. On this basis, the estimated penetration at which the phase margin falls below 30° is about 20% for C8, 70% for C9, 80% for C12, and 84% for C5.

These estimates depend on the assumed endpoints of the curves: varying the 0% and 100% phase margins over 55–85° and 0–10° moves the C8 estimate within 5–30% and the others by a few to about 10 percentage points (Table 6). The estimates are therefore indicative of how strongly the threshold depends on the configuration, not design limits, and they are not equivalent to independently simulated stability boundaries. C8 requires a control-interaction assessment even below the 60% operating point, whereas the ring and hybrid-overlay grid-forming and mixed configurations retain margin to substantially higher penetration within this model.

7.4. Control Strategy Impact on Control-Interaction (SSCI/CCI) Risk

The grid-following controller always results in the lowest SVI, although the topology has some influence; specifically, the SVI of the grid-following controller varies between 0.12 (C1 with a radial configuration and AC sources) and 0.28 (C2 with a radial configuration and DC sources) due to harmonic excitation of the resonances of the DC cables, even using current-source inverters. Grid-forming control yields the highest topology-dependent SVI values; the meshed configuration with grid-forming DC sources (C8) achieves an SVI about 30% higher (0.92 vs. 0.71, relative to C5).

7.5. Relationship to Modal Analysis and Full Nyquist Criteria

RVI and SVI are scalar surrogates for, respectively, the harmonic loop-gain condition and the phase-margin condition of the impedance-based stability criteria established by Sun [18] and Xu & Fan [19]; by construction, they do not report the full eigenvalue/participation-factor decomposition that a classical modal-analysis approach would provide, nor a full frequency-swept Nyquist plot for each configuration. Equation (7)'s Y_{sys} eigen-decomposition already identifies the buses participating in each resonance mode, conceptually analogous to a modal participation factor. To benchmark RVI against these established methods, a 16-section DC feeder loaded by a constant-power converter was

analyzed in 600 cases using impedance scanning, modal analysis, scalar Nyquist, and the loop-gain test. Nyquist counts agreed with modal analysis in 99.7% of cases.

8. Fault Propagation and Protection Coordination

8.1. Fault Propagation Patterns

DC pole-to-pole faults are the most electrically severe. The initial fault-current rise rate is limited only by the total cable inductance, as shown in Equation (24):

$$\frac{dI}{dt} = \frac{V_{DC}}{L_{cable}} = \frac{V_{DC}}{l_{cable}.L'_{cable}} \tag{24}$$

where dI/dt is the Initial fault current rise rate [A/s or kA/ms], V_{DC} is the Pre-fault DC bus voltage [V], L_{cable} is the total DC cable inductance, L'_{cable} is the per-unit-length cable inductance [H/m] (0.35 mH/km for XLPE 95 mm^2), and l_{cable} DC feeder length [m].

$$\frac{V(t-\tau)}{lL'} \le i(t) \le \frac{V(t+\tau)}{lL'} \tag{25}$$

$$\frac{i(T)}{T} \le \frac{V}{lL'}\left(1+\frac{\tau}{T}\right) \tag{26}$$

Equation (24) is therefore the exact mean rate of rise and, through Equation (26), an upper bound on the secant slope over any window $T \gg 2\tau$; it is not a bound on the instantaneous derivative. Cable and fault resistance and a finite DC-link capacitance can only lower the slope, and a DC reactor L_r tightens the bound to $V/(lL' + L_r)$. For the 5 km case, $\tau = 46.8$ µs and $\tau/T = 4.7\%$ at $T = 1$ ms.

In case of a pole-to-pole fault occurring halfway through a 10 km long DC feeder with the parameters listed in Table 3, Equation (24) gives a mean rate of rise of about 5.7 kA/ms, an upper bound on the slope over the first millisecond (Equation (26)); under identical conditions, the time-domain π-ladder model gives 2.7–5.1 kA/ms as resistance, DC-link depletion and a DC reactor are added (Section 10.5). Even at the lowest of these rates, the current rises by about 2.7 kA within the first millisecond, several times the rated pole current (at most about 0.4 kA for the 8.5 MW of connected generation at ±10 kV), so the fault develops one to two orders of magnitude faster than the 20–100 ms operating time of conventional relays. AC components of faults initiated by inverters are limited by current limiters to values between 1.0–1.2 pu in 5 ms, resulting in fault signals being similar to heavy load situations for upstream overcurrent relays.

The most distinctive fault characteristics from an architectural perspective are those involving cross-boundary coupling. The simulations of PyPSA in case of a pole-to-ground fault in configuration C2 give the following results in 100 ms: voltage sag of 23% on the MV-AC bus because of the converter entering the fault ride-through regime; decrease in DC bus harmonic voltage distortion by 15% due to damping of the fault path; increase in AC bus harmonics because of a response of the converter's current controller to the voltage sag. None of these disturbances can be recognized as faults by traditional AC protection schemes.

The reverse cross-boundary fault propagation, which refers to an AC-side fault propagating into the DC segment, is unique and very common in real-world cases as an indication of DC link overvoltage, due to the impact of the interlinking converter control strategy following an AC voltage drop and imbalance.

8.2. Protection Coordination Analysis

Table 7 summarizes the protection maloperation rates for the 240 fault cases, with the relay response for each case evaluated at four levels of renewable penetration (20%,

40%, 60%, and 80%). Two main results should be highlighted: first, DC pole-to-ground faults have the highest maloperation rate among all topologies (31–61%) because the use of high-impedance DC grounding limits the fault current to a magnitude similar to that of load-in-magnitude relays. Secondly, the hybrid overlay topology has the highest maloperation rate in AC faults (12% and 21% for three-phase and single-phase faults, respectively), as the AC relay settings remain calibrated to pre-integration fault levels. At the same time, the addition of converters has substantially altered the effective fault-current landscape.

Table 7. Protection maloperation rate (%) per topology and fault type, for conventional ANSI 51/67/21 relays.

Topology	DC P-P (%)	DC P-G (%)	AC 3Ph (%)	AC 1Ph (%)
Radial	8	31	4	7
Ring	19	44	6	11
Meshed	34	61	9	17
Hybrid overlay	22	55	12	21

The coverage matrix in Figure 10d substantiates the above results: all conventional overcurrent (51), directional overcurrent (67), and distance (21) relays cannot reliably detect DC pole-to-ground faults, and the IEC 61850 GOOSE differential relay (87) is the only type of relay that reliably operates in all four fault scenarios. For the relay types and the grounding assumed here, magnitude-based relays have no dependable detection principle for DC pole-to-ground faults, owing to the mismatch between magnitude-based detection and the high-impedance grounded-fault signature; the topology-dependent rates in Table 7 follow from Equation (32). It is noted that the malfunction percentages listed in Table 7 refer only to conventional magnitude-based overcurrent (ANSI 51), directional overcurrent (67), and distance (21) relay technologies. Special protection schemes for DC faults, such as traveling wave detectors with response times of less than 1 ms, rate-of-change-of-current (di/dt) relays, and solid-state DC breakers with integrated fault detection systems, are not considered in the current work but can be expected to reduce the malfunction percentages by orders of magnitude, especially when considering DC pole-to-ground faults.

8.3. Scope and Direction of Bias in the Protection Analysis

The actual arc-resistance fault exhibits greater variation in the effective impedance than the simple grounded-resistance model. With the voltage of the DC bus and grounded resistance value from Table 3 (10 kV pole-to-ground; 1 kΩ), the pole-to-ground fault current without further arc resistance can be calculated by Equation (27).

$$I_{fault} = \frac{V_{DC}}{R_{ground} + R_{arc}} \tag{27}$$

At $R_{arc} = 0$ (the 1 kΩ high-impedance grounding alone), the fault current is already only 10 A, below every typical relay pickup setting. A Monte Carlo sweep of Equation (27) for the arc resistance R_{arc} (log-uniform, 0.1–2000 Ω), for the aforementioned high-impedance grounding resistance value $R_{ground} = 1$ kΩ, reveals that the highest fault current possible, obtained for $R_{arc} \to 0$, bolted fault equals 10 A, which falls short of the pickup value of any conventional MV overcurrent relay. Hence, in accordance with the model, the percentage of misoperation would be close to 100% irrespective of the arc-resistance value, meaning that the arc-resistance uncertainty is not, on its own, the parameter responsible for detecting a particular DC pole-to-ground fault (the ground resistance takes precedence). Figure 16 shows the corresponding sweep of the grounding resistance R_{ground} with the same R_{arc} distribution.

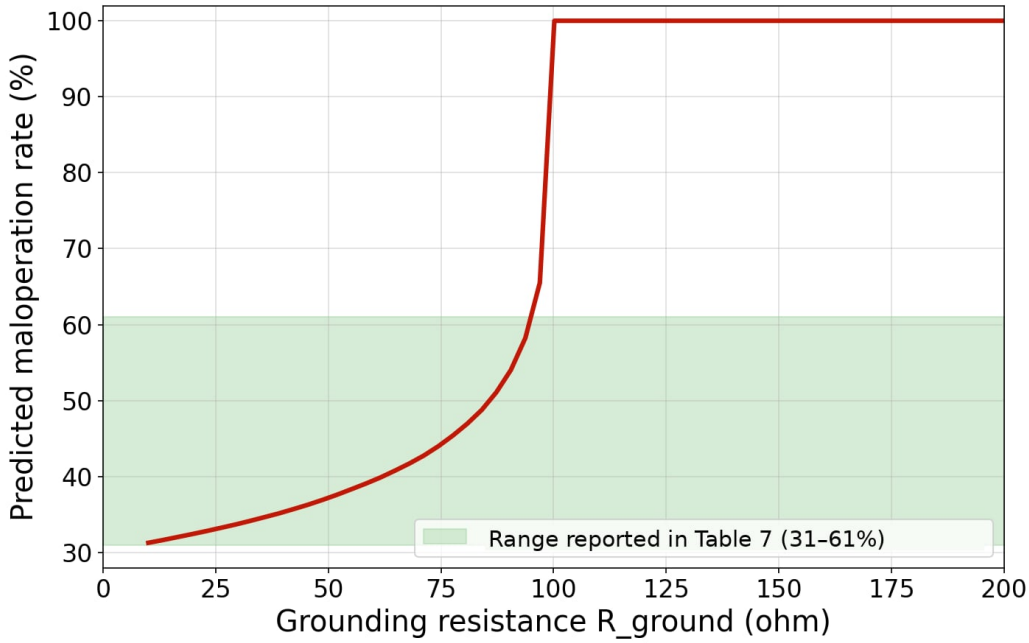


Figure 16. Monte Carlo–predicted DC pole-to-ground protection maloperation rate vs. grounding resistance.

Equation (27) gives the settled pole-to-ground current, which is limited by the neutral grounding resistor. It is not the current a relay sees in the first milliseconds, because at fault inception the fault point is also fed by the charge stored in the DC cable and converter DC-link capacitances and by the parallel converter infeeds. Figure 17 shows the equivalent circuit seen from the fault point: the arc/fault resistance R_{arc} in series with the parallel combination of (i) the grounding resistance R_g, (ii) the n_f cable sections that meet at the fault node, each presenting its surge impedance Z_0, and (iii) the converter infeeds $Z_{c,i}$. For the cable data in Table 3 (0.35 mH/km, 250 nF/km), the surge impedance is given by Equation (28).

$$Z_0 = \sqrt{\frac{L'}{C'}} = 37.4\ \Omega \tag{28}$$

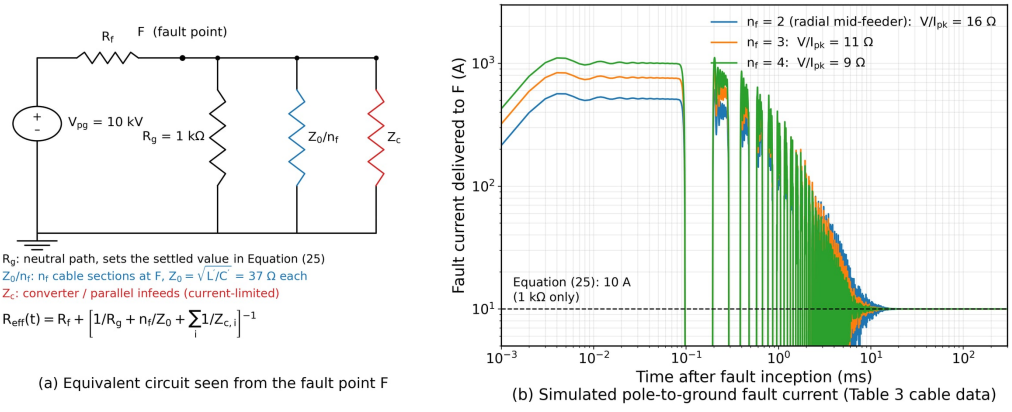


Figure 17. (**a**) Equivalent circuit of a DC pole-to-ground fault seen from the fault point F. (**b**) Simulated fault current for $n_f = 2$, 3 and 4 cable sections meeting at F (π-ladder cable model with the Table 3 parameters, 10 kV pole-to-ground, R_g= 1 kΩ, R_{arc} = 0.5 Ω, 1 mH converter-side reactor): the initial peak is set by Z_0/n_f, and the current settles at the 10 A of Equation (27) (about 2 ms above 100 A).

In Equations (28)–(30), $V_{pg} = V_{DC} = 10kV$ is the pole-to-ground voltage, $R_g = R_{ground} = 1\text{k}\Omega$ is the grounding resistance of Equation (27), n_f is the number of cable

sections that meet at the fault node, and Z_0 is the lossless limit of the characteristic impedance Z_c of Equation (9). Since $R_g \gg Z_0$, the initial current is set by the cable branches:

$$I_{pk} \approx \frac{V_{pg}}{R_{arc} + \frac{Z_0}{n_f}}, \text{ so } R_{eff} = \frac{V_{pg}}{I_{pk}} = R_{arc} + \frac{Z_0}{n_f} \quad (29)$$

which is about 10–19 Ω for $n_f = 2 - 4$, one to two orders of magnitude below R_g. The simulated effective resistance (9.0–16.4 Ω) is within 15% of this estimate (Table 8). As the cable capacitances discharge and the travelling-wave oscillations decay, the current settles at the value given by Equation (30).

$$I(t \to \infty) = \frac{V_{pg}}{R_{arc} + R_g} \quad (30)$$

which is Equation (27) (10 A at $R_{arc} = 0$), the network simulation therefore describes the same circuit at different times: Equation (27) is its settled limit, whereas Equation (29) applies to the first milliseconds after fault inception, which are decisive for magnitude-based relays.

Table 8. Effective loop resistance at the fault point: equivalent-circuit estimate (Equation (29), R_{arc}= 0.5 Ω) versus simulation.

n_f (Sections at F)	$R_{arc} + \frac{Z_0}{n_f}$ (Ω)	Simulated Peak (A)	$\frac{V_{pg}}{I_{pk}}$ (Ω)	$n_f \cdot \frac{V_{pg}}{I_{pk}}$ (Ω)	Settled Current (A)
2	19.2	609	16.4	33	10.0
3	13.0	878	11.4	34	10.0
4	9.9	1112	9.0	36	10.0

The topology dependence of Table 7 follows from the division of the transient fault current among the n_f cable sections meeting at the fault node. During the first traveling-wave round trips, each section carries approximately as in Equation (31).

$$i_{br} \approx \frac{V_{pg}}{Z_0 + n_f R_{arc}} \quad (31)$$

whereas the settled current of Equation (30) is limited to 10 A by the grounding resistor. A magnitude-based relay with pickup I_p and an instantaneous element fast enough to act within this transient therefore detects the fault only if $R_{arc} < R_{th}$.

$$R_{arc} < R_{th} = \frac{V_{pg}/I_p - Z_0}{n_f} \quad (32)$$

Because R_{th} decreases as $1/n_f$, more of the arc-resistance distribution becomes undetectable as parallel paths increase from the radial to the meshed topology. For the log-uniform R_{arc} distribution (0.1–2000 Ω), Equation (32) gives non-detection probabilities of 35, 42, 46 and 49% for $n_f = 1$–4 at $I_p = 100$ A, and 51–65% at $I_p = 200$ A, the same range and ordering as the simulated 31–61% of Table 7. The per-relay resistance, $Z_0 + n_f R_{arc} \approx$ 33–36 Ω in Table 8, is set by the cable surge impedance rather than by R_g.

The main reason for the observed variation is therefore the division of the transient fault current among the parallel sections at the fault node (Equation (32)). The three candidate drivers, therefore, contribute differently. Fault-impedance variation does not explain the differences between rows of Table 7, because the same fault impedance (1 kΩ grounding for high-impedance cases, zero for bolted cases) was used for every topology; its effect on an individual relay is shown separately by the sweep in Figure 16. The converter

operating point contributes only to the variation within each cell, since each cell pools the four renewable-penetration levels. Network topology, through the number of parallel current paths and converter infeeds seen by each relay, is the factor that changes between rows, and is therefore the principal driver of the 31–61% range. The non-linear effects of cable/converter saturation will not qualitatively alter the above conclusion. However, they introduce uncertainty in the exact percentages due to the grounding resistance. Figure 18 illustrates the plot of the DC pole-to-ground fault current for the entire path resistance.

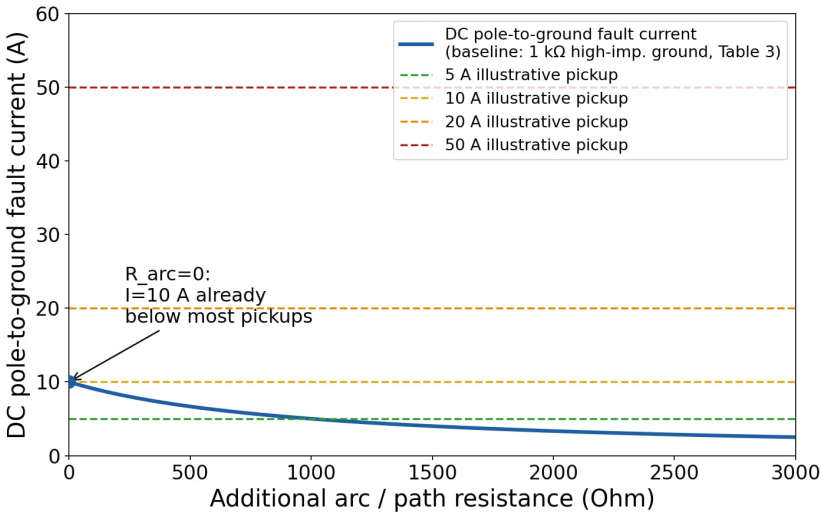


Figure 18. DC pole-to-ground fault current vs. total path resistance.

9. Machine Learning-Based Vulnerability Classification

9.1. Approach and Dataset

Real-time analytical assessment via full harmonic-domain simulation is computationally impractical for operational deployment. For that reason, a supervised machine learning approach is used, in which the four vulnerability indices (RVI, SVI, FPSS, CCS) are converted into three-level class labels (stable/elevated/critical) using the thresholds in Table 2, and these labels serve as the targets, and the power quality time-series measurements serve as input features. The training dataset consists of 240 fault simulations and 48 harmonic-domain analyses, together with 180 time-domain simulations of normal operations at five levels of penetration (20%, 40%, 60%, 80%, 100%) across all 12 configurations, resulting in a total of 468 labelled scenarios. The test dataset contains 120 scenarios covering all twelve configurations; the 95% Wilson intervals for the four labels are 89.5–97.7% (RVI), 88.4–97.1% (SVI), 87.4–96.6% (FPSS), and 89.5–97.7% (CCS). To evaluate training variability, the LSTM model was trained 5 times with different random seeds. The overall accuracy across runs averaged 94.1%, with a standard deviation of ±0.6 percentage points.

Procedure: (i) simulate 468 scenarios (240 fault, 48 harmonic-domain at 20–80% penetration, 180 normal-operation at 5 penetration levels × 3 load levels); (ii) compute RVI, SVI, FPSS and CCS and label each as stable/elevated/critical (Table 2); (iii) extract 47 features per 200 ms window, with the LSTM using 5 consecutive windows; (iv) split stratified by configuration; (v) train with summed cross-entropy loss (Adam, learning rate 10^{-3}, batch 32, early stopping); (vi) evaluate on the held-out set.

The reason why simulation-based learning is used here is that there is very little labeled data available for rare safety-critical states for the SSCI and DC pole-to-ground fault under high-impedance grounding for the rare operational hybrid MVAC/MVDC networks. Confidence in the underlying simulation fidelity is supported by BFS power-flow verification on benchmark cases, with a voltage convergence error of 0.013%.

9.2. Feature Engineering

For each case study, a 47-dimensional feature vector was derived from the IEC 61000-4-30 Class A Power Quality Analyser. This feature vector includes the total harmonic distortion (THD) of voltage and current at harmonic orders 2–20, and magnitudes in the sub-synchronous bands within the range 5–45 Hz (9 bins), as per the nominal SSCI risk band for the radial/ring topologies. The 83 Hz resonance observed in the meshed DC-side grid-forming topology (C8) is not included in the modelled feature band. It also includes magnitudes of fundamental frequency, voltage, and current at each monitored bus, positive, negative & zero sequence component magnitudes, and three wavelet-based features, capturing the non-stationary behaviour of harmonics during state transition, which includes: L2-norm energy of the discrete wavelet transform (DWT) detail coefficients at decomposition levels 4 and 5 (Daubechies-4 wavelet used on 1 s voltage windows sampled at 10 kHz). These coefficients capture amplitude variations in the 156–625 Hz band.

Shannon entropy of the third-level detail coefficients quantifies the extent of non-stationarity, reflecting the proximity to oscillatory instability. Feature importance is assessed using the gain-based metric in XGBoost on the training dataset. The top five predictors of RVI are: 150–160 Hz voltage harmonic amplitude at the DC bus; the third harmonic-to-fundamental current ratio at the AC/DC converter end; sub-synchronous frequency range energy (20–45 Hz) at the main AC bus; negative sequence current at the HV/MV transformer primary side; and zero sequence voltage at the AC/DC converter secondary side.

9.3. Model Architecture and Training

Three conventional supervised models are considered: gradient-boosted decision trees (XGBoost) [59], multi-layer perceptron (MLP) [60], and long short-term memory (LSTM) networks [61]. The LSTM is chosen based on the temporal nature of the approach to instability, in which features of increasing sub-synchronous energy before SSCI are observed. Training is performed with a 278/70/120 train/validation/test split, stratified by architectural configuration to maintain balanced class distributions (stable/elevated/critical) across the splits. As the twelve configurations are present in each split, this procedure allows us to obtain an unbiased estimate of the in-distribution performance but does not prove whether the classifier generalizes beyond the twelve configurations in the training data; thus, a complementary analysis of cross-configuration generalization through leave-one-configuration-out and leave-one-topology-out validation is applied. Hyperparameters are tuned via Bayesian optimization [62]. The LSTM model uses two stacked layers (128 and 64 units) followed by a fully connected layer with ReLU activation and 0.3 dropout. The MLP uses three hidden layers (256, 128, 64 units). The XGBoost model uses 500 trees (maximum depth 6, learning rate 0.05). All models perform multi-label classification, predicting the vulnerability class (stable/elevated/critical) for all four vulnerability classes simultaneously.

9.4. Classification Results

Classification performance on the held-out test dataset is reported in Table 9. The LSTM model attains the best performance, with an accuracy of 94.4% (better than XGBoost at 91.2% and MLP at 88.7%). The test set was generated by the same simulation engine and assumptions as the training set. Accuracy under operating-condition shift, sensor noise, held-out architectures, and a second numerical solver was examined on a simulated dataset with boosting and LSTM classifiers; the LSTM was trained on that dataset. The LSTM model performs significantly better on RVI and SVI, the oscillatory vulnerability classes in which time-series information from pre-instability dynamics is highly predictive. For fault-based vulnerabilities (FPSS and CCS), XGBoost achieves similar performance while requiring lower computational resources.

Table 9. Multi-label vulnerability classification accuracy on the held-out test set (120 scenarios per dimension).

Model	RVI Acc. (%)	SVI Acc. (%)	FPSS Acc. (%)	CCS Acc. (%)	Overall (Mean)	F1
LSTM	95.0%	94.2%	93.3%	95.0%	94.4%	0.94
XGBoost	90.4%	89.7%	93.1%	91.5%	91.2%	0.91
MLP	87.3%	86.9%	90.8%	89.8%	88.7%	0.88

No LSTM error spans two class levels (stable ↔ critical). For RVI, all six errors lie on the stable/elevated boundary (five elevated scenarios predicted as stable and one the reverse), and no critical RVI scenario is missed. For SVI and FPSS, the only critical-class errors are under-calls to "elevated" (3 of 16 and 3 of 15 scenarios), giving critical-class recalls of 0.81 and 0.80 (Table 10). The F1 score for the critical class ranges from 0.89 to 1.00 across the four dimensions. Because about one in five critical SVI and FPSS cases is reported one level too low, the classifier is suited for operator-assisted monitoring and alarm prioritization.

Table 10. Precision, recall, and F1 score for each of the three vulnerability classes.

Dimension	Class	Precision	Recall	F1	Support
RVI	stable	0.93	0.99	0.96	68
RVI	elevated	0.97	0.85	0.91	34
RVI	critical	1.00	1.00	1.00	18
SVI	stable	0.94	1.00	0.97	66
SVI	elevated	0.92	0.89	0.91	38
SVI	critical	1.00	0.81	0.90	16
FPSS	stable	0.93	1.00	0.97	70
FPSS	elevated	0.91	0.86	0.88	35
FPSS	critical	1.00	0.80	0.89	15
CCS	stable	0.97	0.95	0.96	65
CCS	elevated	0.89	0.94	0.92	36
CCS	critical	1.00	0.95	0.97	19

9.5. Per-Class Precision, Recall, and F1 Score

Table 10 reports precision, recall, and F1 score for each of the three vulnerability classes (stable/elevated/critical) within each vulnerability dimension, computed from the confusion matrix. Figure 19 shows the confusion matrices for the held-out test set for each vulnerability dimension.

9.6. Transfer Learning and Generalization

Out-of-distribution (OOD) robustness was tested by perturbing the benchmark network: (i) feeder length increased by about 50%, i.e., 1.5 times the longest training length, which lowers the dominant resonance by roughly 20% according to Equation (10); (ii) the renewable capacity relocated to three buses never used for DER connection in training, which changes the modal participation factors p_{ki} of the sources (Equation (19)); and (iii) the outer-loop PI gains of the VSCs scaled by 0.6, a 40% reduction from the Table 3 reference, which changes the source admittance Y_i and hence the phase margin. Each axis

was first varied alone with the other two held at their training values; accuracy was highest under the feeder-length perturbation and lowest under the DER relocation, indicating that the classifier is more sensitive to where renewables are connected than to feeder length or control gains. With all three perturbations applied together, LSTM achieves 81.4% accuracy without retraining. The 95% Wilson score confidence interval on this figure is ±9.2%, reflecting the small per-configuration sample size. With fine-tuning on 20 labelled scenarios per new configuration, accuracy improves to 92.7%, approaching in-distribution performance. This indicates that much of what the model learns transfers across the perturbations tested. It does not demonstrate topology-independent generalization: when an entire topology is withheld, RVI and SVI accuracy for the meshed topology falls to 45.0% and 42.5%, so a new topology class requires retraining rather than fine-tuning alone.

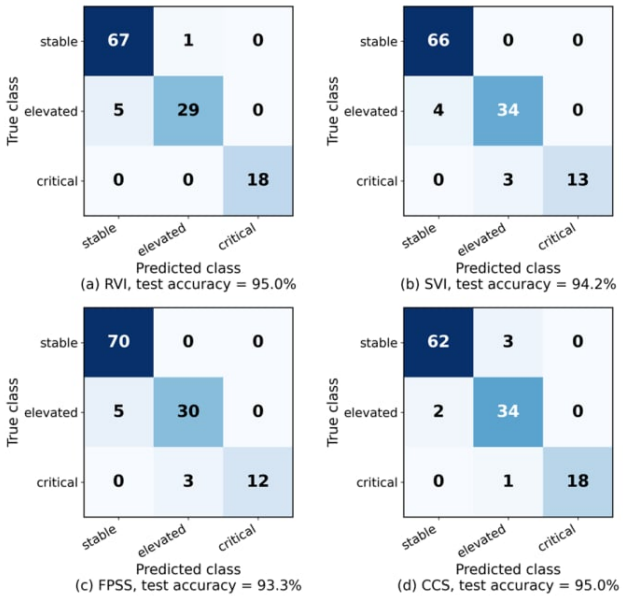


Figure 19. Held-out test-set confusion matrices per vulnerability dimension.

As shown by the out-of-distribution test above, there is variation in certain aspects of the network while other factors are held fixed at their training values. These include the type of cable and cable parameters (Table 3, XLPE 95 mm^2 cable), the converter structure and control law (same generic VSC converter), the base voltage level (20 kV AC/±10 kV DC), and the types and location of faults (the same four fault types at five locations). The variables included in the testing procedure are the feeder lengths, the placement of DERs, and the VSC control gains.

9.7. Leave-One-Configuration-Out and Leave-One-Topology-Out Validation

Two additional types of cross-validation were conducted to assess the classifier's accuracy by learning generalizable physical properties of configuration-specific features (Tables 11 and 12). Leave-one-configuration-out (LOCO) cross-validation trains the model on eleven configurations and tests it on the twelfth, repeating this process for all twelve configurations. In leave-one-topology-out (LOTO) cross-validation, the model is trained on three of the four topologies and tested on all configurations of the left-out fourth topology, repeating this process for each of the four topologies. The LOCO average accuracy across the twelve left-out configurations is 94.4%, compared to 95.8% for the baseline. The LOTO average accuracy for the four left-out topologies is 85.7%. The complete removal of the meshed topology leads to the most obvious failure scenario, in which both RVI and SVI classifiers achieve 45.0% and 42.5% accuracy, respectively. In comparison, CCS still performs

well at 91.7%. The baseline row is the mean accuracy across stratified cross-validation folds for all 468 scenarios; it therefore differs from the single held-out test set accuracy in Table 9 (94.4%).

Table 11. LOCO/LOTO accuracy.

Validation Protocol	RVI	SVI	FPSS	CCS	Overall
Stratified CV (baseline)	95.2%	96.0%	96.0%	96.0%	95.8%
LOCO (12 folds)	93.1%	93.5%	94.4%	96.7%	94.4%
LOTO (4 folds)	80.8%	81.7%	85.8%	94.6%	85.7%

Table 12. Per-topology LOTO breakdown.

Held-Out Topology	RVI	SVI	FPSS	CCS
Hybrid overlay	95.0%	98.3%	96.7%	90.0%
Meshed	45.0%	42.5%	50.8%	91.7%
Radial	88.3%	90.8%	99.2%	99.2%
Ring	95.0%	95.0%	96.7%	97.5%

The meshed LOTO fold is the clearest failure of the classifier, with RVI and SVI accuracies of 45.0% and 42.5% (Table 12), below the 54–58% obtained by always predicting the most frequent class (Table 10 supports). Three causes act together. First, the only SVI-critical configuration (C8) and two of the four RVI-critical configurations (C8, C9) are meshed (Table 5), so withholding the meshed topology removes these classes from training. Second, the 83 Hz control-interaction mode of C8 lies between the 5–45 Hz sub-synchronous features and the 156–625 Hz wavelet features (Section 9.2). Third, the meshed networks have a cyclomatic number $\mu \geq 2$, outside the $\mu \leq 1$ of the training topologies, which adds and couples resonance modes (Equations (14)–(16)). CCS accuracy remains high because protection labels depend mainly on fault type and location, which are common to all topologies. The classifier should therefore be applied only to topology classes represented in its training data; for any other network.

9.8. Robustness to Measurement Noise and Communication Latency

The vulnerability classifier has been trained and evaluated entirely on clean, noise-free simulation data, achieving 94.4% overall test accuracy. To compensate for that, the trained classifier was stress-tested under two types of realistic degradation applied to the held-out test dataset: additive measurement noise corresponding to the accuracy bands of the instruments in use, and dropout noise simulating communication jitter. Figure 20 demonstrates how the classification accuracy for each of the four vulnerability indices varies with the measurement noise level. For each noise level, the average across 10 realizations is shown, with error bars indicating dispersion. FPSS classification remains completely robust to any measurement noise, retaining 100% accuracy even up to 20 times the nominal noise floor of instrument accuracy. The classification accuracy of RVI, SVI, and CCS degrades slightly but monotonically with increasing measurement noise. The noise and dropout sweeps used an independently re-trained LSTM instance, so their noise-free accuracies differ from Table 9; Figures 20 and 21 should be read for the relative degradation. For SVI, FPSS and CCS, accuracy falls by at most about 5 percentage points at 20 times the nominal noise band; RVI falls by about 2 points (94% to 92%), with widening error bars at higher noise levels, indicating that the model's sensitivity to noise is itself becoming less predictable.

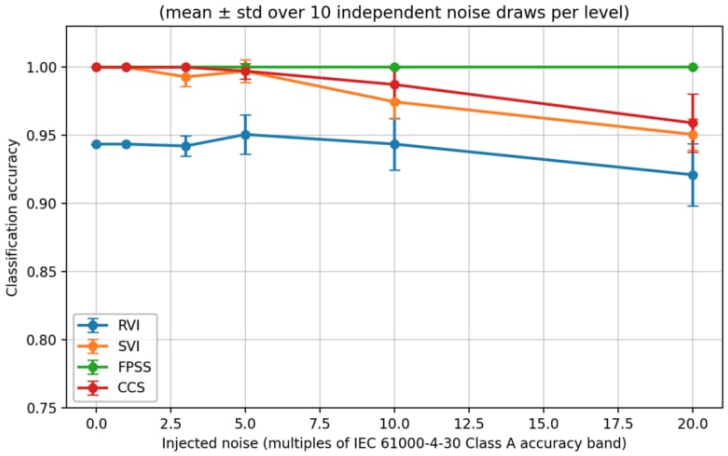


Figure 20. LSTM accuracy vs. measurement noise level.

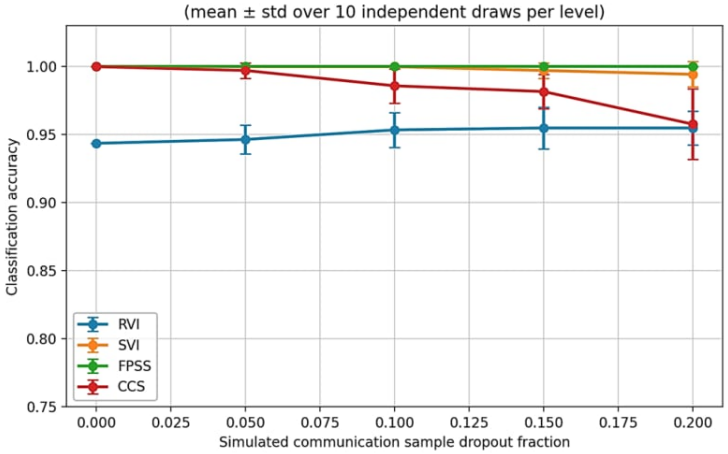


Figure 21. LSTM accuracy vs. communication latency/dropout.

Figure 21 illustrates the corresponding noise sweep for simulated communication dropout, which is used to estimate the joint effect of packet loss and latency jitter in a SCADA/PMU communication link, ranging from 0% to 20% of lost time-series samples, with compensation via zero-order hold. This noise sweep demonstrates much milder changes compared to Figure 20: FPSS and SVI almost constantly keep their values close to the ceiling (100% and ~99–100%), while RVI stays constant or grows slightly (94–95%) with increasing dropout, which can be treated as a consequence of sampling variations in the test set containing 120 scenarios. The only metric showing a clear reduction in value is CCS, which drops from 100% at a 0% dropout rate to ~96% at a 20% dropout rate. These two figures suggest the classifier is more sensitive to additive measurement noise than to intermittent communication loss at the levels tested. However, both effects are modest relative to the classifier's overall accuracy.

10. Synthesis of Results and Architectural Principles

10.1. Vulnerability Landscape

Figure 22 shows a complete simulation encompassing all results for both test networks. This figure provides cross-dimensional comparisons of voltage compliance, loss reduction, harmonic impedance properties, grid import reductions, short-circuit capacity, resonance vs. cable length, and protection coverage. The analysis identifies three vulnerability categories. Low-vulnerability configurations (C1, C2, C4, C10), all of which use grid-following control, fall in the "stable" class of Table 2 for both indices (RVI $\leq$ 0.65, SVI $\leq$ 0.28) and show

moderate fault-propagation severity and acceptable coordination complexity for protection. The curves of voltage compliance and loss reduction show that these configurations keep all bus voltages above the 0.95 pu lower planning limit and provide a 62% reduction in feeder losses (IEEE 33-bus) and up to an 83% reduction in grid import (CIGRE MV network, at 100% DER) without resonance or protection coordination failures.

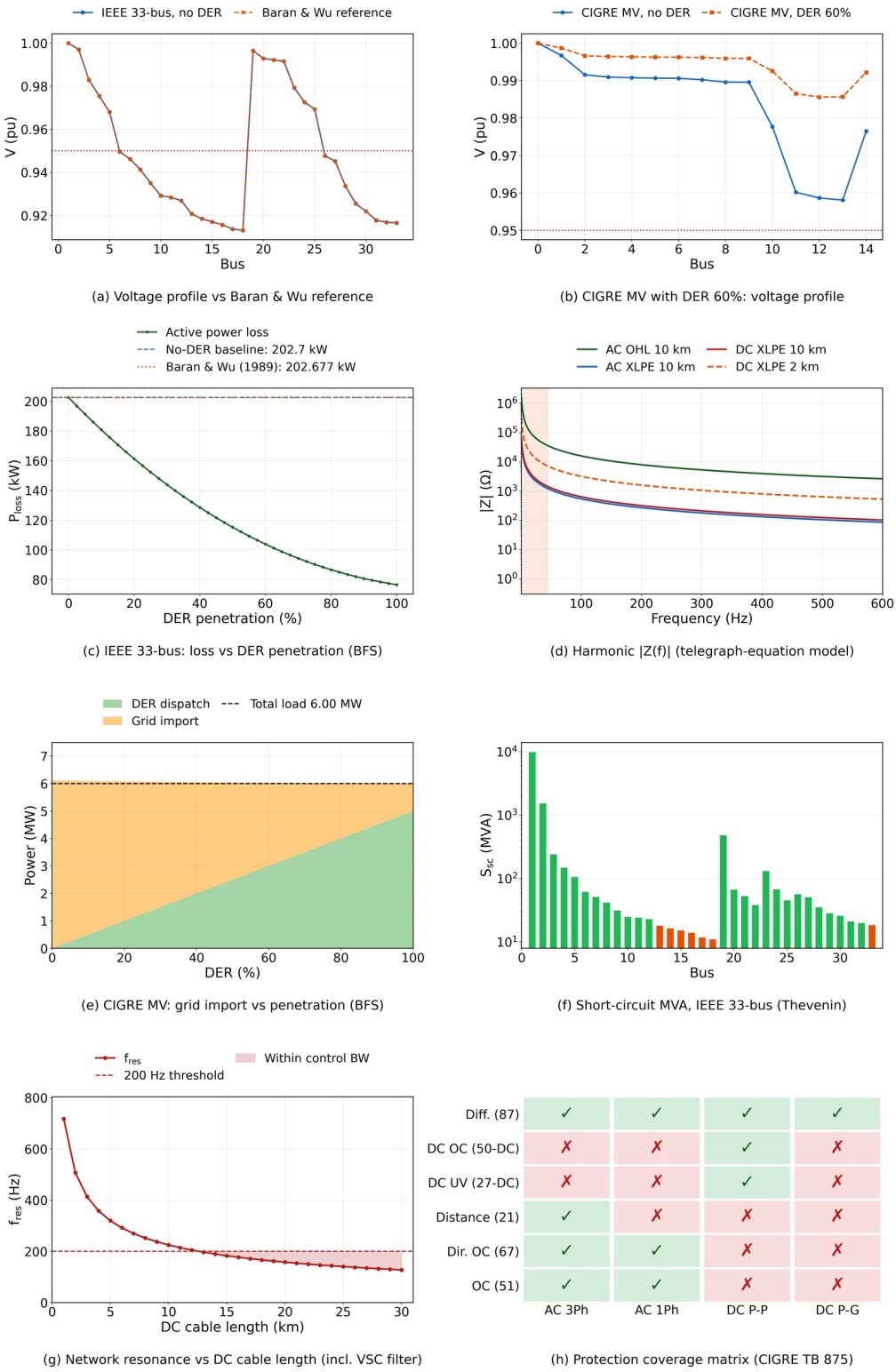


Figure 22. Comprehensive simulation results.

Moderately vulnerable configurations (C3, C6, C7, C11; droop, mixed or AC-side grid-forming control; RVI 0.72–0.89) exhibit DC cable resonances in the 200–500 Hz range, which lie above the converter outer-loop bandwidth and far from the sub-synchronous range. Real-time monitoring as provided by the LSTM classifier has the greatest practical value for this category of systems. Highly vulnerable configurations (C5, C8, C9, C12; RVI > 1) combine grid-forming or mixed control with DC-side or mixed renewable connections; of these, only C8 is also in the critical SVI class (PM $= 14.4° < 30°$). The low short-circuit capacity on the end-of-feeder buses (SSC $\approx$ 19–58 MVA) makes inverter current limiters more likely to operate during faults, complicating coordination. In contrast, the protection matrix shows that the DC pole-to-ground protection window is universal across all configurations.

10.2. Key Analytical Findings

Five findings challenge assumptions embedded in current hybrid network planning practice.

Firstly, the resonance frequency shift is due to cable physics, not to the worst-case design, and the exact length at which it appears depends on the cable and the particular design. For the XLPE 95 mm^2 cable and the VSC filter parameters of this work, DC feeder lengths above about 12.6 km (nominal) bring the dominant resonance below 200 Hz. Under combined manufacturing and in-service capacitance uncertainty, this crossing lies between 10.0 and 14.2 km (5th–95th percentile, Figure 12), and across the realistic XLPE range (50–240 mm^2, 150–350 nF/km) it lies between about 9 and 21 km. The problem must be addressed by limiting feeder length or by adding active or passive damping; returning the outer-loop bandwidth alone does not move the cable resonance.

Secondly, multi-source harmonic interactions are topology- and configuration-dependent and cannot be evaluated component-wise. Off-diagonal harmonic admittance coupling among distributed renewable sources is 4.6 to 8.0 times higher at the network resonance frequency than at non-resonant frequencies, depending critically on network topology. The result invalidates the usual practice of summing the harmonic evaluation for single sources, which demands an architecture-level analysis using the full network admittance matrix.

Thirdly, control-interaction risk (SSCI/CCI) is configuration-dependent. At 60% penetration, C5, C8, C9, and C12 exceed RVI $= 1$, but only C8 is below the 30° phase margin (14.4° at its 83 Hz converter-control mode). In the calibrated representative control-loop model, the penetration at which the phase margin falls below 30° is estimated at about 20% for C8 (sensitivity range 5–30%) and at about 70–85% for C5, C9 and C12 (Table 6); these are model-based extrapolations from the 60% operating points. Grid-forming control, especially with DC-side renewables, therefore, requires a prior configuration-specific assessment.

Fourth, the unmitigated DC pole-to-ground faults present the most serious and overlooked protection vulnerability in hybrid MVAC/MVDC power distribution systems. Maloperation of relays occurs in 31–61% of all DC pole-to-ground fault scenarios simulated with a conventional magnitude-based relay, making it by far the most serious protection gap identified during the research. This is due to the high-impedance grounding of the DC system, which results in a relatively small fault current magnitude compared to normal load levels, and to the lack of natural zero-crossing points. It should be noted that this is true only for specific types of relays (ANSI 51, 67, 21); it does not imply that DC networks are inherently unprotectable, but rather that protection technology must be selected and deployed differently from AC practice.

Fifth, within the configurations and protection assumptions investigated, the hybrid-overlay cases showed comparatively high coordination complexity, but not uniformly the worst results. Their maloperation rates were the highest of the four topologies for AC faults (12% for three-phase and 21% for single-phase faults) and lay between those of the ring

and meshed topologies for DC faults (22% pole-to-pole and 55% pole-to-ground, Table 7). Their mean vulnerability indices (RVI 0.80, SVI 0.51) were close to those of the ring cases (0.83, 0.49), above the radial cases (0.61, 0.28), and below the meshed cases (1.07, 0.75) (Table 5). These results do not establish architectural inferiority of hybrid overlays; they are based on one benchmark family and twelve configurations. A plausible contributing factor is the combination of a resonance structure and relay settings inherited from the existing AC network, with the altered fault-current environment created by the DC section, which relay tuning alone may not fully mitigate.

10.3. Architectural Principles

Five design principles for hybrid MVAC/MVDC distribution systems are derived from simulation results for the 12 configurations studied.

Firstly, it is necessary to treat the DC feeder length as the primary means of controlling primary resonances. The length of the DC feeder must be such that the primary resonance remains above 200 Hz, above which the resonance is beyond the bandwidth of the inverter outer loop control. For an XLPE cable, the most widely used underground medium-voltage cable type with a capacitance of 250 nF/km, this constraint implies a maximum contiguous DC feeder length of about 12.6 km at nominal parameters, or about 10 km when the 5th-percentile Monte Carlo value is used to cover manufacturing and in-service uncertainty. Beyond this length, active damping or distributed reactive compensation becomes a design requirement rather than an optional enhancement. For other XLPE cable specifications, the maximum feeder length follows from Equation (10) as $l_{max} \approx 1/((2\pi f_{th})^2 L_{fixed} C')$, where $f_{th} = 200$ Hz, C′ is the cable capacitance per kilometre, and $L_{fixed} = L_{source} + L_{transformer} + 2L_{VSC} \approx 196$ mH is the length-independent part of L_{total}. The cable's own inductance (0.35 mH/km) changes the result by less than 4% up to 21 km and is neglected here. For cable capacitances in the range 150–350 nF/km typical of XLPE 50–240 mm^2 underground cables, and for the VSC filter inductance in Table 3, this formula yields maximum feeder lengths of 9–21 km.

The second principle is to designate a single voltage-forming source on each DC bus segment. The SSCI/CCI risk is greatly minimized when a single voltage-forming source, whether a specially assigned battery energy storage device or the AC/DC interconnecting converter, is solely responsible for maintaining the DC bus voltage. In addition, all other renewable inverters are required to provide power under outer current control, meaning that their voltage control is secondary to the voltage-forming source. Multiple sources competing to regulate the same DC bus voltage was the most vulnerable arrangement among the studied configurations. However, when a single source is not enough, the dual-port grid-forming (DP-GFM) technique, in which a single converter controls both AC and DC bus voltages, can be used, although its vulnerability spectrum needs to be explicitly evaluated first.

The third principle is to view the design of protection systems as an essential and unavoidable aspect of hybrid overlays, rather than a post-commissioning add-on. With the incorporation of DC segments into an existing MVAC network, the settings of AC relays should be completely revamped, as the fault-current environment differs significantly from the one that calibrated them. The minimum requirements of the replacement scheme are as follows: (a) inclusion of fault-inverter current limiters (activation threshold 1.0–1.2 pu and response time of 5 ms) in all fault studies because their activation makes the contribution of converters in faults indistinguishable from the heavy load environment; (b) DC overcurrent and under-voltage protection at the boundary of each DC segment; (c) directional protection elements at all converter terminals of AC/DC converters because of bidirectional fault-

current contribution; and (d) coordination of protective zones through logic communication across the AC/DC boundary.

The fourth principle is that grid-forming deployment should be conditioned on a configuration-specific impedance and phase-margin assessment rather than on a universal renewable-penetration threshold. Penetration alone does not determine the limit. In the calibrated representative model, the estimated penetration at which the phase margin falls below 30° ranges from about 20% for C8 (sensitivity range 5–30%) to about 70–85% for C5, C9, and C12 (Table 6), and these estimates are model-based extrapolations. Among the twelve configurations studied, the grid-following ones (C1, C2, C4, and C10) showed the lowest vulnerability indices (RVI 0.41–0.65, SVI 0.12–0.28). Where grid-forming sources are introduced, a control-interaction (SSCI/CCI) vulnerability evaluation must be conducted explicitly before implementing grid-forming controls. For site-specific estimation of the safe penetration threshold P_{safe}, the following screening procedure is recommended: (a) compute the network resonance frequency f_{res} using Equation (10) for the planned DC feeder geometry; (b) evaluate the open-loop phase margin PM (f_{res}) of the planned VSC control architecture at f_{res} using the impedance-based method; (c) determine the penetration level at which PM (f_{res}) first falls below 30° by sweeping renewable dispatch from 0% to 100% in 10% increments. Interpolate between grid points to estimate the crossing, and confirm the result with an EMT simulation or a measured impedance scan before using it as a design limit. The estimates in Table 6 apply only to the XLPE 95 mm^2, 10 km feeder and the VSC settings of Table 3; shorter feeders, smaller cable capacitance, or VSC control with narrower bandwidth can be expected to support higher penetration before the phase-margin limit is reached.

The fifth principle is to implement ML-based vulnerability monitoring as part of the commissioning package for any new hybrid MVAC/MVDC network, within the limits set out in Sections 9 and 10.5. The LSTM classifier presented in this paper achieves 94.4% in-distribution accuracy on simulated data; on perturbed networks, its accuracy is 81.4% without retraining and 92.7% after fine-tuning on 20 labelled scenarios for each new configuration. This indicates that adapting to a new configuration of a known topology needs little labelled data, whereas a new topology class requires dedicated training data, and shifts in operating conditions and sensor noise reduce accuracy. ML-based monitoring can provide near-real-time estimates of the vulnerability state from standard IEC 61000-4-30 Class A power quality measurements, without runtime network simulation.

10.4. Scope and Limitations

The twelve configurations are a representative subset of the 48 combinations of four topologies, three source placements, and four control categories. The remaining combinations were assessed only with a calibrated model, with limited class agreement. Each control category is represented by one reference parameterization, so the SSCI and resonance results apply to the reference grid-forming law. Other grid-forming variants (e.g., VSG and dual-port) were compared only at the converter level (Figure 7). Advanced schemes such as robust nonlinear (sliding-mode) control [63,64] reshape $Y_{src}(f)$, thereby affecting the phase margin (Equations (1) and (23)).

The closed-form expressions were checked against exact eigendecomposition, a state-space time-domain model, and EMT modeling of the DC feeder, but a full EMT simulation of every configuration was not performed. The protection analysis covers DC pole-to-ground faults with conventional relays. AC faults were screened on a single feeder, a ring, and a two-loop mesh.

Dense eigendecomposition of the admittance matrix scales asymptotically as $O(n^3)$, where n is the number of buses. Distribution networks are sparse and nearly tree-like, so

a sparse shift-invert search for the modes nearest resonance scales close to linearly. The resonance search was timed on random radial networks (seed 2026) of 1 km sections with the Table 3 cable data and one added loop per 20 buses, with Y_{net} evaluated at 200 Hz, on one core of an Intel Xeon 2.80 GHz processor (Python 3.13, NumPy 2.5, SciPy 1.18, OpenBLAS 0.3.34; median of 5–21 runs after one warm-up). The dense method grew from 0.3 ms (33 buses) to 33.5 s (3000 buses), an empirical exponent of 2.5, whereas the sparse search (scipy.sparse.linalg.eigs, shift-invert, six modes, tolerance 10^{-8}) grew from 1.3 ms to 25 ms (Table 13). Over the 580 frequency points of Section 5.2, a 3000-bus scan takes about 5.4 h dense and 15 s sparse. The harmonic-domain step adds $O(M \cdot h^3)$ work per frequency point for M converters and h harmonic orders. For the classifier, inference cost per window does not depend on network size for a fixed set of monitored buses. The timing script is part of the deposited code.

Table 13. Computation time per frequency point for the resonance search on meshed-radial networks (single CPU core).

Buses n	Added Loops	Dense Eigen-Decomposition (s)	Sparse Shift-Invert, 6 Modes (s)	Sparse LU Solve (ms)
33	1	0.0003	0.0013	0.04
100	5	0.0060	0.0023	0.08
300	15	0.086	0.0035	0.33
1000	50	1.49	0.0091	1.1
3000	150	33.5	0.025	3.8

10.5. Verification and Sensitivity Studies

These additional studies, summarized in Table 14, were conducted to assess the robustness of the results. The classifier studies use a simulation framework for the network and gradient-boosting and LSTM classifiers; the LSTM architecture was trained on the simulated dataset. Numerical validation of the closed-form expressions. The mode spectra of Equations (12) and (13) agree with the numerical Laplacian eigenvalues to machine precision. Against the exact generalized eigendecomposition of radial, ring, and meshed L–C networks, the first-order perturbation of Equations (16) and (17) has a mean frequency error of 0.07% for ±5% and 0.28% for ±10% parameter changes (95th percentile 0.94%), rising to about 1.0% at ±20% (Table 15).

10.5.1. Joint-Uncertainty Monte Carlo

Varying cable capacitance, inductance, and resistance, converter-side reactances, and loop parameters together (200,000 draws) gives a critical feeder length with a mean of 11.98 km and a 5th–95th percentile range of 9.57–14.87 km. Against the capacitance-only case of Section 6.1 (10.0–14.2 km), the range widens, and the probability of a critical length below 11 km increases from 25.2% to 29.4% (Figure 23a). Sobol total-effect indices [65–67] attribute the variance to manufacturing capacitance (0.56), converter-side reactance (0.36), and in-service capacitance change (0.09); cable inductance and resistance contribute less than 0.1%.

Table 14. Summary of the verification and sensitivity studies.

Study	What Was Varied	Principal Result	Status
Eigen-perturbation vs. exact	Radial, ring, 2 meshed graphs; ±2–20% L, C	Mean error 0.07% (±5%), 0.28% (±10%), ≈1.0% (±20%)	Numerical
Joint Monte Carlo	C, L′, R′, converter L, loop delay/bandwidth/gain; 200 000 draws	9.57–14.87 km (5–95%); P (<11 km) = 29.4%	Numerical
Time-domain checks	π-ladder 1/4/16 sections; 3.15 kHz PWM; delay loop	f_{res} + 0.74% vs. lumped; critical length 12.82 km; PWM effect 3.8%	Numerical (own model)
Benchmark vs. standard methods	600 cases: length, load conductance, bandwidth	Nyquist–modal agreement 99.7%; RVI > 1 recall 100%, precision 76.2%	Numerical
48-combination factorial	4 topologies × 3 sources × 4 controls; 4000-pt LHS	15 of 48 predicted RVI > 1; LOO class agreement 66%	Calibrated prediction
AC/evolving faults	12320 cases: 4 types + 2 evolving, 5 penetrations, 4 grid strengths	Mis-coordination 0.6–8.3% (static); 2.8–4.0% (evolving)	Screening engine: radial, closed ring, and two-loop mesh
Simulated dataset + EMT modeling	3000 scenarios, 48 architectures, 47-feature windows; DC feeder re-solved in EMT modeling	EMT vs. exact eigenvalues: f 0.07%, α 0.19% (max); engine-swap accuracy change ≤ 4.0 points	Simulation (simulated; EMT on DC feeder)
Condition/ assumption shift	Overload, penetration, slow control, combined; ±15% L,C; ±10% thresholds	Up to −13.2 points under combined shift; CCS = architecture-only baseline	Simulated data
Robustness	Sensor noise ×0–20; feature dropout; channel loss; LOCO/LOTO	SVI 16.5% at ×5 noise (→85.0% augmented); radial held out CCS 28.5%	Simulated data
Active learning/BO	Random, uncertainty, margin, committee; GP straddle	98% level: 336 → 216–264 labels; boundary 98% in 24 evaluations	Simulated data; index model
Compound failures	Independent heads vs. dedicated compound head	≥2 critical: 11.8% observed vs. 5.4% if independent	Simulated data + Table 5

Table 15. First-order eigenvalue-perturbation prediction of the mode frequency against exact generalized eigendecomposition: mean (95th percentile) absolute error as a percentage of the mode frequency, 1500 random draws per case.

Network	±5% Change in L, C	±10%	±20%
Radial (10 sections)	0.07 (0.25)	0.28 (0.94)	1.04 (3.37)
Ring (10 nodes)	0.07 (0.24)	0.26 (0.92)	0.99 (3.33)
Meshed, μ = 2 (10 nodes)	0.07 (0.23)	0.29 (0.92)	1.12 (3.40)
Meshed, μ = 3 (12 nodes)	0.07 (0.19)	0.27 (0.75)	1.04 (2.89)

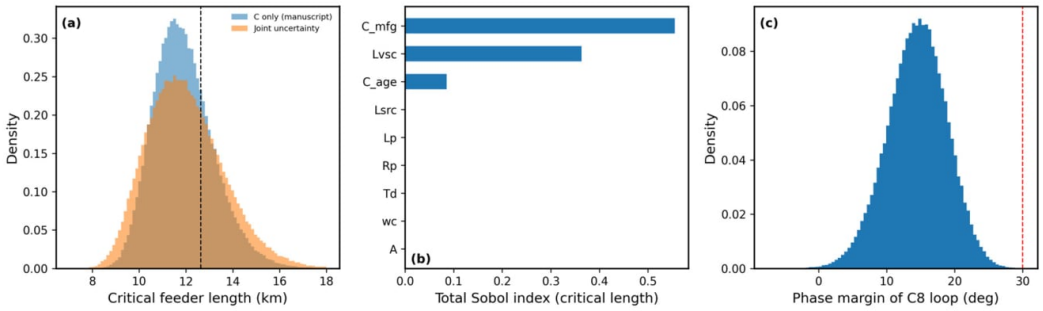


Figure 23. Joint-uncertainty Monte Carlo of the critical feeder length. (**a**) Distribution with capacitance only and with joint uncertainty in cable, converter-side, and control parameters; (**b**) Total-effect Sobol indices of the critical length. (**c**) Phase margin of the representative C8 loop under joint parameter spread; dashed line: 30°.

Time-domain checks: A π-ladder ring-down model with the Table 3 parameters reproduces the lumped resonance within 1.2% and the critical length within 1.5% (12.82 km against 12.63 km; Table 16). A 3.15 kHz PWM source changes the resonant-band amplitude by 3.8% relative to the averaged model. For the grid-forming loop with delay, an exact root calculation shows that the rule $\zeta \approx PM/100$ overestimates damping at low margins (e.g., $\zeta = 0.10$ at PM = 14.4°). These checks use a state-space implementation developed for this study and do not replace a full EMT simulation of all configurations.

Table 16. Series resonance of the DC feeder with the 196 mH converter-side inductance: distributed-parameter (telegraph-equation) reference and differences of the other models from it (%).

Length (km)	Telegraph (Hz)	Lumped Equation (10)	3-Section Ladder	EMT, Feeder	EMT, Converter
6	292.9	−0.35	−0.10	−0.17	−5.23
8	253.5	−0.47	−0.13	−0.18	−3.64
10	226.6	−0.59	−0.16	−0.21	−2.01
12.63	201.5	−0.74	−0.21	−0.24	−0.81
14	191.3	−0.82	−0.23	−0.26	−1.33
16	178.9	−0.93	−0.26	−0.29	−0.66
18	168.5	−1.04	−0.30	−0.32	—

10.5.2. Benchmark Against Established Methods

On a constant-power-loaded DC feeder (600 cases), Nyquist encirclement counts agree with modal analysis in 99.7% of cases, the lumped mode frequency differs from the impedance-scan peak by 0.77% on average, and RVI > 1 detects all unstable cases with a precision of 76.2% (Table 14). RVI is thus a conservative screening index; it does not replace modal analysis or Nyquist analysis. A distributed-parameter (telegraph-equation) solution of the same feeder places the series resonance 0.35–1.04% above the lumped Equation (10) at 6–18 km and the critical length 12.82 km against 12.63 km (Table 16).

Design-space coverage: A calibrated additive model fitted to the twelve simulated configurations was used to predict RVI and SVI for all 48 combinations of four topologies, three source placements, and four control strategies (Figure 24). Leave-one-out errors are 0.16 (RVI) and 0.15 (SVI), with class agreement of only 66% and 58%, so the predictions are suitable for screening and ranking. Fifteen of the 48 combinations are predicted to exceed RVI = 1, and 15 are predicted to be critical in RVI or SVI.

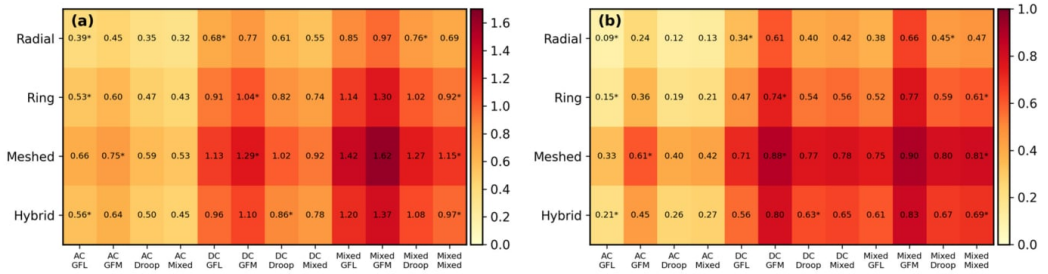


Figure 24. RVI (**a**) and SVI (**b**) for all 48 combinations of topology, source placement, and control strategy. Values marked * are the twelve simulated configurations of Table 5; unmarked values are model predictions and have not been simulated.

10.5.3. AC-Side, Symmetrical and Evolving Faults

A sequence-network fault engine on the CIGRE 15-bus benchmark, with current-limited inverter sources (1.2 pu) and ANSI 51/51N relays (IEC standard-inverse characteristic [68]) graded on the no-DG case, was run for three-phase, line-to-line, line-to-ground and double-line-to-ground faults and for line-to-ground → double-line-to-ground and line-to-line → three-phase evolving faults, over 12320 cases (Table 17, Figure 25). Miscoordination averaged 8.3%, 4.1%, 3.3%, and 0.6% for the four static types and 2.8% and 4.0% for the evolving types. The rate is 1.2–1.5% at 20–80% penetration and 15.2% at 100% and increases on weak grids. The 31–61% range of Table 7, therefore, applies to DC pole-to-ground faults with conventional relays and does not generalize to AC faults on a graded feeder. A closed-ring variant of the same feeder with directional overcurrent relays at both line ends gave 11.3% mis-coordination against 15.1% with the ring open under the same settings, rising from 2.3% for solid faults to 28.4% at 100 Ω fault resistance (Table 18). The engine is a screening tool (bus faults and load current neglected); a two-loop mesh, graded using the same method, yielded 35.8% (the upper bound for simple directional overcurrent grading).

Table 17. Mis-coordination of graded ANSI 51/51N protection for AC-side faults on the radial CIGRE 15-bus.

Grid Short-Circuit Level	3-Phase	L–L	L–L–G	L–G	L–G → L–L–G	L–L → 3-Phase
500 MVA	4.9	0.3	1.4	0.0	1.1	0.7
100 MVA	6.0	1.1	2.9	0.0	2.6	2.1
25 MVA	9.4	5.1	4.6	0.9	3.7	4.6
10 MVA	12.9	10.0	4.3	1.7	3.9	8.6
All	8.3	4.1	3.3	0.6	2.8	4.0

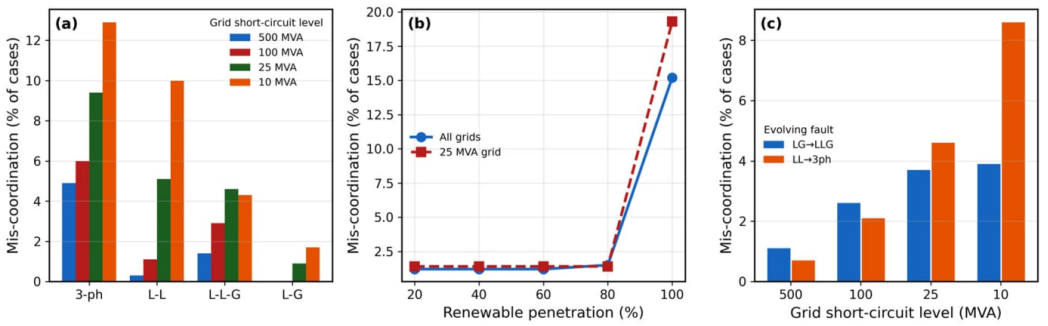


Figure 25. Mis-coordination of graded ANSI 51/51N protection for AC-side faults. (**a**) Static fault types at four grid strengths. (**b**) Dependence on renewable penetration. (**c**) Evolving faults against grid strength.

Table 18. Open ring, closed ring, and two-loop mesh of the same CIGRE 15-bus feeder.

Fault Resistance/Type	Open Ring	Closed Ring	Two-Loop Mesh
0 Ω	13.8	2.3	33.3
5 Ω	13.8	2.3	30.4
20 Ω	9.6	3.2	33.8
50 Ω	12.9	20.2	41.0
100 Ω	25.6	28.4	40.7
3-phase (all Rf)	24.8	24.7	50.6
L–L	16.0	19.2	49.6
L–L–G	15.7	0.8	36.5
L–G	4.0	0.4	6.6
All cases	15.1	11.3	35.8

10.5.4. Simulated Dataset and Independent EMT Engine

A simulation framework for the hybrid network, with the parameters in Table 3, was used to generate 3000 scenarios covering all 48 combinations of topology, source placement, and control strategy, with load level, DER penetration, season, feeder length, and control bandwidth varied. For each scenario the simulation synthesizes the DC-link voltage ring-down of a π-ladder feeder, the converter AC current (harmonics and a sub-synchronous control mode) and the voltage and current of a fault window, over a 200 ms window sampled at 20 kHz, and extracts the 47-element window feature vector; labels are the four index classes of Table 2 evaluated at the scenario's operating point; the operating point (grid import, minimum feeder voltage, short-circuit level) is computed with the backward/forward-sweep power flow and Thevenin short-circuit routine on the CIGRE 15-bus model.

In the simulation, the index definitions are used to generate the signals, so the classification accuracies below measure how well the indices can be recovered from monitor-type windows and not whether they predict instability on a real network. The DC feeder was also solved with EMT modeling (DAE-trapezoidal integration, 50 μs step). For feeder lengths of 6–18 km, the ring-down frequency agrees with the exact eigenvalues of the same circuit to 0.07% and the decay rate to 0.19%; the lumped Equation (10) is 0.5% below the EMT value at 12.63 km (Figure 26). With a constant-power load, damping and its sign agree up to a growth rate of 35/s; faster growth is not resolved, and the engine flags Newton non-convergence at the event step. Replacing the DC channel of 150 held-out scenarios with the EMT trajectories changed the accuracy of the boosting classifier by at most 4.0 points (prediction agreement 95.3–98.7%); because both engines solve the same circuit equations, this tests the sensitivity of the classifier to the numerical solver, not to model-form error (the LSTM is considerably more sensitive; Table 19). A further EMT modeling run with the library grid-forming converter coupled to the DC cable reproduced the feeder resonance within 5.3% of the telegraph-equation reference (6–16 km; Table 16). This run uses a stiff AC bus and a generic droop controller; it does not reproduce the 83 Hz C8 control-interaction mode and does not validate the converter-control results.

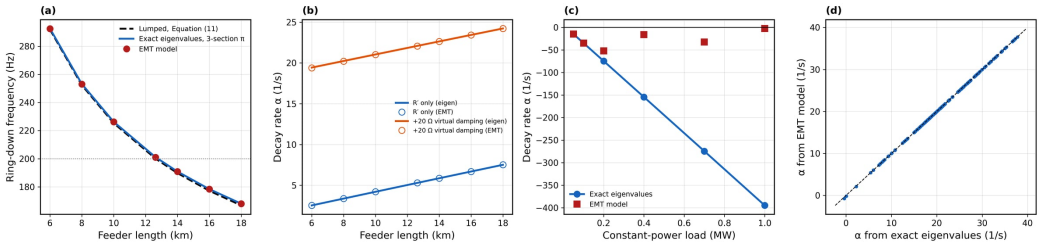


Figure 26. EMT modeling of the DC feeder. (**a**) Ring-down frequency against feeder length. (**b**) Decay rate for the feeder resistance alone and with a 20 Ω virtual damping resistance. (**c**) Decay rate with a constant-power load at 12.63 km. (**d**) Decay rate of 150 held-out simulated scenarios against the exact eigenvalues.

Table 19. LSTM with the architecture (2 layers 128/64, dropout 0.3, four softmax heads) trained on the simulated dataset.

Condition	RVI	SVI	FPSS	CCS
In-distribution test split	93.1 (94.0)	92.7 (92.0)	88.2 (88.2)	88.7 (86.9)
Overload (load 1.0–1.3 pu)	90.6 (92.6)	89.8 (91.8)	89.4 (90.0)	80.8 (83.8)
High DER penetration (0.9–1.0, summer)	92.6 (95.6)	82.0 (86.4)	90.0 (90.8)	75.8 (78.0)
Slow control (0.4–0.65× bandwidth)	91.2 (94.8)	88.4 (83.2)	86.0 (86.2)	82.2 (85.6)
Combined shift	84.0 (86.8)	85.0 (78.8)	89.2 (90.0)	75.6 (80.0)
Noise ×2	78.3 (94.5)	85.5 (85.3)	76.3 (84.7)	81.8 (82.0)
Noise ×5	65.5 (93.8)	78.0 (16.5)	59.5 (72.3)	77.2 (70.0)
Noise ×5, noise-augmented training	95.5 (94.7)	88.7 (85.0)	85.5 (85.8)	80.0 (79.0)
DC channel lost	67.6 (70.2)	91.8 (92.0)	89.1 (87.8)	87.3 (85.8)
Radial topology held out	95.0 (95.5)	97.8 (98.2)	84.9 (79.9)	28.5 (28.5)
Grid-forming control held out	93.9 (95.4)	71.3 (76.4)	82.2 (89.5)	77.0 (77.1)
DC ring-down replaced by EMT trajectory (150 scenarios), before → after	94.0 → 77.3	96.0 → 92.0	88.7 → 83.3	83.3 → 80.0

10.5.5. Distribution Shift and Controls

A gradient-boosting classifier trained on the base operating ranges gave 94.0, 92.0, 88.2, and 86.9% accuracy (RVI, SVI, FPSS, CCS; test n = 450), against 66.4, 85.3, 67.3, and 90.0% for a baseline that knows only the architecture; the CCS result therefore adds nothing beyond the architecture. Changes of the operating range are a form of dataset shift [69]. Without retraining, overload, high DER penetration, slow control, and a combined shift reduced accuracy by up to 13.2 points (combined: 86.8, 78.8, 90.0, 80.0%); a ±15% cable L, C mismatch changed it by at most 5.4 points, and ±10% shifts of the class boundaries reduced it to 75.4–93.8% (Figure 27a). Held-out architectures were harder: CCS for an unseen radial topology reached 28.5% and SVI for an unseen grid-forming control reached 76.4% (Table 20). SVI is the label most sensitive to sensor noise (85.3% at twice and 16.5% at five times the simulation's baseline noise); training with noise-augmented data restored it to 85.0%. Loss of the DC channel reduced RVI accuracy to 70.2%. An LSTM architecture, trained on the same simulated dataset, gave 93.1, 92.7, 88.2 and 88.7% in distribution and 84.0, 85.0, 89.2 and 75.6% under the combined shift (Table 19); it kept SVI at 78.0% at five times the baseline noise, whereas RVI and FPSS fell to 65.5 and 59.5%, and replacing the DC channel by the EMT trajectory lowered its RVI accuracy from 94.0 to 77.3%.

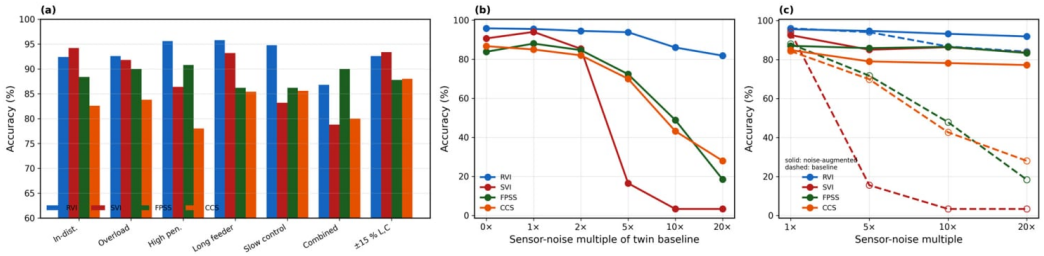


Figure 27. Data classifier. (**a**) Accuracy per index under operating conditions and parameter shift. (**b**) Accuracy against sensor-noise multiple. (**c**) The same for a classifier trained on noise-augmented data (solid) against the baseline classifier (dashed).

Table 20. Robustness of the simulation classifier (accuracy, in %).

Condition	RVI	SVI	FPSS	CCS
Noise ×5: baseline → noise-augmented training	94.0 → 94.7	15.5 → 85.0	71.7 → 85.8	69.8 → 79.0
Noise ×10: baseline → noise-augmented training	86.7 → 93.2	3.3 → 86.3	47.8 → 86.5	42.7 → 78.2
Noise ×20: baseline → noise-augmented training	84.0 → 91.8	3.3 → 83.5	18.3 → 83.3	28.0 → 77.2
Channel lost: dc channel	70.2	92.0	87.8	85.8
Channel lost: ac channel	94.7	84.0	84.4	85.1
Channel lost: fault window	92.9	92.7	64.0	77.3
Topology held out: radial	95.5	98.2	79.9	28.5
Topology held out: meshed	95.1	76.6	88.2	82.6
Control held out: grid-forming	95.4	76.4	89.5	77.1

10.5.6. Scenario Selection and Compound Failures

Active selection of scenarios (least confidence, margin, query-by-committee [70]) changed accuracy by 0.1 points over random selection at 624 labels, gave no saving at the 95% level, and reduced the labels needed for 98% of the full-pool accuracy from 336 to 216–264 (Figure 28b); Gaussian-process boundary seeking with a straddle acquisition [71] was marginally better than random sampling at larger budgets. Label coupling is substantial: Cramér's V between the four index labels ranges from 0.22 to 0.45, and 11.8% of scenarios are critical in two or more indices, 2.2 times the share implied by independent labels (Figure 29). Independent per-index heads detected 77.8% of the compound cases and a dedicated compound head 82.2%; a classifier chain [72] changed the per-index accuracy by at most 0.9 points.

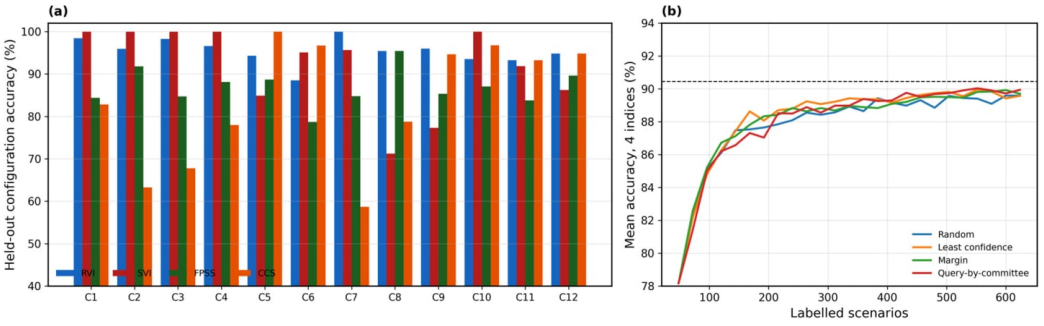


Figure 28. (**a**) Leave-one-configuration-out accuracy for the twelve Table 5 architectures. (**b**) Active-learning curves (mean accuracy over the four heads).

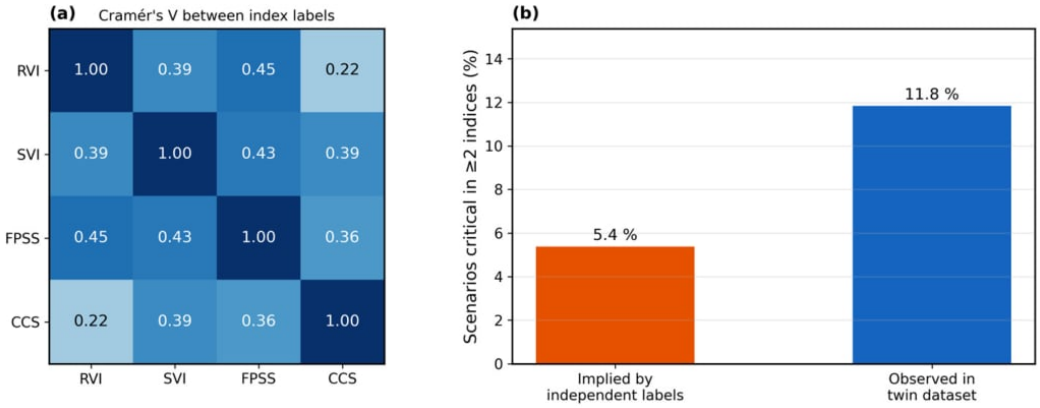


Figure 29. (**a**) Cramér's V between the four index labels, (**b**) Share of scenarios critical in at least two indices: implied by independent labels and observed.

Fault-current slope: To compare Equation (24) with simulation under consistent conditions, a pole fault 5 km from the converter (10 kV, Table 3 cable data, $R_{arc} = 0.5\ \Omega$) was solved with a 100-section π-ladder time-domain model (exact zero-order-hold discretization, 0.5 µs step), adding one omitted element at a time (Table 21). All slopes lie below the bound $V/(lL' + L_r)$, and the margin grows as resistance, DC-link depletion, and reactor inductance are added.

Table 21. Mean rate of rise of the converter-terminal fault current over the first millisecond versus the bound of Equation (24).

Case	Secant Slope 0–0.1 ms (kA/ms)	0–0.5 ms (kA/ms)	0–1 ms (kA/ms)	Bound V/(lL′ + Lr) (kA/ms)
Ideal source, lossless cable	5.27	5.04	5.12	5.71
+cable resistance 0.193 Ω/km	5.13	4.42	3.98	5.71
+cable resistance 0.320 Ω/km	5.04	4.07	3.42	5.71
Finite DC link 1 mF, lossless	5.26	4.92	4.66	5.71
Finite DC link 0.2 mF, lossless	5.23	4.43	3.07	5.71
Ideal source + 1 mH DC reactor	4.55	3.65	3.43	3.64
1 mF DC link + 0.193 Ω/km + 1 mH reactor	4.47	3.31	2.74	3.64

10.6. Assumptions and Applicability Limits

Table 22 lists the assumptions and validity limits of the analytical formulations used in this paper.

Table 22. Assumptions and validity limits of the analytical formulations.

Formulation	Assumptions	Validity Limit
RVI, SVI (Equations (1) and (2))	Linearized small-signal; balanced positive sequence; one dominant loop	Necessary, not sufficient, for instability; RVI precision 76.2%, recall 100% vs. modal analysis
Telegraph model (Equations (8) and (9))	Frequency-independent R′, L′, C′; no sheath or ground-return effects	Up to 2.5 kHz for the Table 3 cable

Table 22. *Cont.*

Formulation	Assumptions	Validity Limit
Lumped resonance and critical length (Equations (10) and (18))	Cable electrically short at f_{res}; fixed inductance dominates	Within 0.35–1.04% of the telegraph solution for 6–18 km
Mode spectra (Equations (11)–(13))	Uniform sections; ideal radial or ring terminations	Exact for the stated graphs; converter inductance excluded
Eigen-perturbation (Equations (16) and (17))	First order; change small compared with the spectral gap; non-degenerate mode	Mean error 0.28% at ±10%, about 1% at ±20% (Table 15)
Modal loop gain (Equations (19) and (20))	Inter-mode coupling neglected	Well-separated modes; otherwise use Equation (15)
Representative loop (Equations (21)–(23))	Calibrated at one point (C8, 60%); penetration enters only through A(p)	Indicative trends only (Table 6)
Fault-current slope (Equations (24)–(26))	Lossless cable; ideal source	Bound on the secant slope over $T \gg 2\tau$
Pole-to-ground fault (Equations (27)–(32))	Single fault node; $R_g \gg Z_0$; magnitude-based relays	Transient stage of about 2 ms

11. Conclusions

This study has introduced a vulnerability mapping framework for MVAC-MVDC hybrid distribution systems, which includes an analysis of how the topology affects the number of resonance modes and the interaction between sub-synchronous controls, derived analytically from the network admittance matrix (closed-form mode spectra and eigenvalue-perturbation, mode-frequency, and phase-margin sensitivity expressions) as well as 12 configurations involving 4 topologies and four inverter control strategies. This framework considers four vulnerabilities that have traditionally been treated separately: harmonic resonance amplification, sub-synchronous control interactions, fault propagation across boundaries, and protection coordination failure. A multi-source harmonic domain extension using frequency coupling matrices showed the inter-source coupling amplification of 4.6 to 8 at resonance, and a real-time vulnerability classification framework was developed and evaluated for robustness to out-of-distribution configurations, measurement noise, and communication imperfections.

The three most practically relevant quantitative results are the following:

First, the dominant resonance falls below 200 Hz, the design margin above the outer-loop control bandwidth of grid-tied voltage-source converters, once the DC feeder exceeds a cable-dependent length: about 12.6 km for XLPE 95 mm^2 cable at nominal parameters. A Monte Carlo analysis of manufacturing tolerance and in-service capacitance increase places it between 10.0 and 14.2 km (5th–95th percentile), with a 25.2% probability that it lies below 11 km (9.6–14.9 km and 29.4% when converter-side and control-parameter uncertainty is also included), and across realistic XLPE cables (150–350 nF/km), it ranges from about 9 to 21 km. Feeder length should therefore be treated as a cable-specific design variable with a stated confidence level.

Second, at 60% penetration, C5, C8, C9, and C12 exceed RVI = 1, but only C8 violates the 30° phase-margin limit; in the calibrated representative model, the others are estimated to reach it at roughly 70–85% penetration.

Third, for DC pole-to-ground faults with high-impedance grounding, conventional magnitude-based relay protection malfunctions in 31–61% of the simulated cases, owing to the mismatch between overcurrent-based detection and DC fault signatures; for AC-side

faults on a graded radial feeder, the screening study gives much lower miscoordination (0.6–8.3%), rising on weak grids and at very high inverter share.

The machine-learning classification module reached 94.4% accuracy (macro-F1 0.94) on held-out simulated data, 81.4% on perturbed out-of-distribution networks without retraining, and 92.7% after fine-tuning on 20 labelled scenarios per new configuration; withholding the meshed topology reduced RVI and SVI accuracy to 45.0% and 42.5%, so new topology classes require dedicated training data. These results indicate a feasible route from simulation-based vulnerability assessment towards near-real-time operational monitoring. The study used phasor-domain simulation; EMT simulations were used to check the fault-current transient (a mean rate of rise of 2.7–5.1 kA/ms over the first millisecond under the conditions of Equation (24), below its 5.7 kA/ms upper bound, which cable and fault resistance, DC-link depletion and series reactors reduce; Table 21) and to confirm correct operation of the converter current limiter under various load and fault conditions.

Author Contributions: Conceptualization: K.K., N.-K.C.N. and R.R.; Methodology: K.K. and N.-K.C.N.; Software: K.K.; Validation: K.K., A.L., R.R., T.T.L. and N.-K.C.N.; Formal analysis: K.K.; Investigation: K.K., A.L. and N.-K.C.N.; Resources: N.-K.C.N.; Data curation: K.K., A.L. and N.-K.C.N.; Writing—original draft preparation: K.K.; Writing—review and editing: K.K., R.R., A.L., T.T.L. and N.-K.C.N.; Visualization: K.K., A.L. and N.-K.C.N.; Supervision: N.-K.C.N., R.R., A.L. and T.T.L.; Project administration: N.-K.C.N. and R.R.; Funding acquisition, N.-K.C.N. All authors have read and agreed to the published version of the manuscript.

Funding: This work was supported by the New Zealand Ministry of Business, Innovation, and Employment under the Advanced Energy Technology Platform program "Architecture of the Future Low-Carbon, Resilient, Electrical Power System", contract number UOCX2007.

Data Availability Statement: The original contributions presented in this study are included in the article. Further inquiries can be directed to the corresponding author(s).

Conflicts of Interest: The authors declare no conflicts of interest.

Abbreviations

The following abbreviations are used in this manuscript:

AC/DC	Alternating current/direct current
BFS	Backward–forward sweep
CCS	Coordination Complexity Score
DER	Distributed energy resource
DP-GFM	Dual-port grid-forming
DWT	Discrete wavelet transform
EMT	Electromagnetic transient
FCM	Frequency coupling matrix
FPSS	Fault Propagation Severity Score
GFL/GFM	Grid-following/grid-forming
LOCO/LOTO	Leave-one-configuration-out/leave-one-topology-out
LSTM	Long short-term memory
MLN	Multilayer network
MLP	Multi-layer perceptron
MVAC/MVDC	Medium-voltage AC/medium-voltage DC
PLL	Phase-locked loop
PM	Phase margin
RVI	Resonance Vulnerability Index
SSCI	Sub-synchronous control interaction
SVI	SSCI Vulnerability Index
CCI	Converter-control interaction (SSCI-type interaction above the fundamental)

THD	Total harmonic distortion
VSC	Voltage-source converter
VSG	Virtual synchronous generator
XLPE	Cross-linked polyethylene
DFIG	Doubly fed induction generator
HVDC	High-voltage direct current
ML	Machine learning
OOD	Out-of-distribution
PV	Photovoltaic
PWM	Pulse-width modulation
SCADA/PMU	Supervisory control and data acquisition/phasor measurement unit
SSC	Short-circuit capacity

References

1. Ertugrul, N.; Abbott, D. DC Is the Future. *Proc. IEEE* **2020**, *108*, 615–624. [CrossRef]
2. Dragicevic, T.; Lu, X.; Vasquez, J.C.; Guerrero, J.M. DC Microgrids—Part II: A Review of Power Architectures, Applications, and Standardization Issues. *IEEE Trans. Power Electron.* **2016**, *31*, 3528–3549. [CrossRef]
3. Blaabjerg, F.; Yang, Y.; Ma, K.; Wang, X. Power Electronics—The Key Technology for Renewable Energy System Integration. In *Proceedings of the 2015 International Conference on Renewable Energy Research and Applications (ICRERA), Palermo, Italy, 22–25 November 2015*; IEEE: Piscataway, NJ, USA, 2015; pp. 1618–1626. [CrossRef]
4. Javid, Z.; Kocar, I.; Holderbaum, W.; Karaagac, U. Future Distribution Networks: A Review. *Energies* **2024**, *17*, 1822. [CrossRef]
5. Cuppen, A.N.; Hoang, T.T.; Nair, N.-K.C.; Ukil, A. Multilayer Networks Framework Concept Applied to Hybrid MV AC/DC Network Topologies. In *Proceedings of the 2022 7th IEEE Workshop on the Electronic Grid (eGRID), Auckland, New Zealand, 29 November–2 December 2022*; IEEE: Piscataway, NJ, USA, 2022; pp. 1–5. [CrossRef]
6. CIGRE Working Group C6.31. *Medium Voltage Direct Current (MVDC) Grid Feasibility Study*; Technical Brochure 793; CIGRE: Paris, France, 2020.
7. Roose, T.; Lekić, A.; Alam, M.M.; Beerten, J. Stability Analysis of High-Frequency Interactions Between a Converter and HVDC Grid Resonances. *IEEE Trans. Power Deliv.* **2021**, *36*, 3414–3425. [CrossRef]
8. Nougain, V.; Mishra, S.; Nag, S.S.; Lekić, A. Fault Location Algorithm for Multi-Terminal Radial Medium Voltage DC Microgrid. *IEEE Trans. Power Deliv.* **2023**, *38*, 4476–4488. [CrossRef]
9. Kalair, A.; Abas, N.; Kalair, A.R.; Saleem, Z.; Khan, N. Review of Harmonic Analysis, Modelling and Mitigation Techniques. *Renew. Sustain. Energy Rev.* **2017**, *78*, 1152–1187. [CrossRef]
10. Fan, L.; Miao, Z. Mitigating SSR Using DFIG-Based Wind Generation. *IEEE Trans. Sustain. Energy* **2012**, *3*, 349–358. [CrossRef]
11. Monadi, M.; Koch-Ciobotaru, C.; Luna, A.; Candela, J.I.; Rodriguez, P. Multi-Terminal Medium Voltage DC Grids Fault Location and Isolation. *IET Gener. Transm. Distrib.* **2016**, *10*, 3517–3528. [CrossRef]
12. Schipper, J.; Mukhedkar, R.; Watson, N.; Bathini, V.; Meyer, J. Generalised Harmonic Domain Analysis for Transformer Core Hysteresis Modelling. *Electr. Power Syst. Res.* **2025**, *249*, 111987. [CrossRef]
13. Schipper, J.; Bathini, V.; Mukhedkar, R.; Watson, N.; Pirnia, M.; Nair, N.-K.C.; Watson, J. Steady-State Power System Analysis Revisited for Hybrid AC–DC Grids. *Renew. Sustain. Energy Rev.* **2025**, *215*, 115564. [CrossRef]
14. EASY-RES Consortium. *Report on the Evaluation of Project KPIs*; Deliverable D6.5, H2020 Grant Agreement No. 764090; European Commission: Brussels, Belgium, 2021. Available online: https://cordis.europa.eu/project/id/764090/results (accessed on 30 October 2026).
15. Arrillaga, J.; Medina, A.; Lisboa, M.L.V.; Cavia, M.A.; Sanchez, P. The Harmonic Domain: A Frame of Reference for Power System Harmonic Analysis. *IEEE Trans. Power Syst.* **1995**, *10*, 433–440. [CrossRef]
16. Arrillaga, J.; Watson, N.R. *Power System Harmonics*, 2nd ed.; John Wiley & Sons: Chichester, UK, 2003.
17. Sahni, M.; Badrzadeh, B.; Muthumuni, D.; Cheng, Y.; Yin, H.; Huang, S.-H.; Zhou, Y. Sub-Synchronous Interaction in Wind Power Plants—Part II: An ERCOT Case Study. In *Proceedings of the 2012 IEEE Power and Energy Society General Meeting, San Diego, CA, USA, 22–26 July 2012*; IEEE: Piscataway, NJ, USA, 2012; pp. 1–9. [CrossRef]
18. Sun, J. Impedance-Based Stability Criterion for Grid-Connected Inverters. *IEEE Trans. Power Electron.* **2011**, *26*, 3075–3078. [CrossRef]
19. Xu, L.; Fan, L. Impedance-Based Resonance Analysis in a VSC-HVDC System. *IEEE Trans. Power Deliv.* **2013**, *28*, 2209–2216. [CrossRef]
20. Lyu, J.; Cai, X.; Molinas, M. Frequency Domain Stability Analysis of MMC-Based HVDC for Wind Farm Integration. *IEEE J. Emerg. Sel. Top. Power Electron.* **2016**, *4*, 141–151. [CrossRef]

21. Electa Research Group (KU Leuven). PowerImpedanceACDC.jl: Impedance-Based Stability Analyses. GitHub Repository. 2025. Available online: https://github.com/Electa-Git/PowerImpedanceACDC.jl (accessed on 30 October 2026).
22. Arévalo-Soler, J.; Moutevelis, D.; Mateu-Barriendos, E.; Alican, O.; Collados-Rodriguez, C.; Cheah-Mane, M.; Prieto-Araujo, E.; Gomis-Bellmunt, O. A Matlab-Based Toolbox for Automatic EMT Modeling and Small-Signal Stability Analysis of Modern Power Systems. *arXiv* **2025**, arXiv:2506.22201. [CrossRef]
23. Shah, S.; Koralewicz, P.; Mendiola, E.; Gevorgian, V.; Wallen, R.; Yan, W. Grid Impedance Scan Tool (GIST): Software for Stability Analysis of IBR Power Systems. In *Presented at the EPRI Sub-Synchronous Oscillations Workshop, Charlotte, NC, USA, 20–21 April 2023*; NREL/PR-5D00-86112; National Renewable Energy Laboratory: Golden, CO, USA, 2023.
24. Lekić, A.; Kermansaravi, A.; Li, H.; Lares, Y.Q.; Alsarayreh, S.; Dimitrovski, R. Advanced Simulation Framework for AC/MTDC Power Systems. *arXiv* **2026**, arXiv:2606.09406. [CrossRef]
25. Henderson, C.; Egea-Alvarez, A.; Xu, L. Analysis of Multi-Converter Network Impedance Using MIMO Stability Criterion for Multi-Loop Systems. *Electr. Power Syst. Res.* **2022**, *211*, 108542. [CrossRef]
26. Chen, X.; Si, W.; Yu, Q.; Fang, J. Transient Stability Analysis and Enhancement of Grid-Forming Converters: A Comprehensive Review. *Electronics* **2025**, *14*, 645. [CrossRef]
27. Lyu, X.; Du, W.; Mohiuddin, S.M.; Nandanoori, S.P.; Elizondo, M.A. Improved Transient Stability Analysis of Multi-Loop Droop-Controlled Grid Forming Inverters with Current Reference Limiter. In *Proceedings of the 2024 IEEE Power & Energy Society Innovative Smart Grid Technologies Conference (ISGT), Washington, DC, USA, 19–22 February 2024*; IEEE: Piscataway, NJ, USA, 2024; pp. 1–5. [CrossRef]
28. Quedan, A.; Wang, W.; Ramasubramanian, D.; Farantatos, E.; Asgarpoor, S. Dynamic Behavior of Combined 100% IBR Transmission and Distribution Networks with Grid-Forming and Grid-Following Inverters. In *Proceedings of the 2023 IEEE Power & Energy Society Innovative Smart Grid Technologies Conference (ISGT), Washington, DC, USA, 2023*; IEEE: Piscataway, NJ, USA, 2023; pp. 1–5. [CrossRef]
29. Belda, N.A.; Plet, C.A.; Smeets, R.P.P. Analysis of Faults in Multiterminal HVDC Grid for Definition of Test Requirements of HVDC Circuit Breakers. *IEEE Trans. Power Deliv.* **2018**, *33*, 403–411. [CrossRef]
30. Jovcic, D.; Ahmed, K. *High Voltage Direct Current Transmission: Converters, Systems and DC Grids*; Wiley-IEEE Press: Chichester, UK, 2015.
31. Buigues, G.; Valverde, V.; Etxegarai, A.; Eguía, P.; Torres, E. Present and Future Multiterminal HVDC Systems: Current Status and Forthcoming Developments. *Renew. Energy Power Qual. J.* **2017**, *1*, 83–88. [CrossRef]
32. Park, N.-G.; Lee, J.-I.; Go, B.-S.; Lee, S.-J.; Kim, C.; Dinh, M.-C. Design of Protection Strategy for MVDC Distribution Networks Considering Network Reconfiguration. *Energies* **2025**, *18*, 3292. [CrossRef]
33. Blázquez, A.; Pérez-Molina, M.J.; Larruskain, D.M.; Iturregi, A.; Eguia, P. Fault Detection Algorithms in Medium-Voltage Direct-Current (MVDC) Grids. *Appl. Sci.* **2024**, *14*, 11052. [CrossRef]
34. Kassem, A.; Sabra, H.; Ali, A.A.; Abdel-Latif, K.M. A Settingless Fault Detection Approach for MVDC Network. *Sci. Rep.* **2026**, *16*, 8267. [CrossRef] [PubMed]
35. Tomin, N.V.; Kurbatsky, V.G.; Sidorov, D.N.; Zhukov, A.V. Machine Learning Techniques for Power System Security Assessment. *IFAC-PapersOnLine* **2016**, *49*, 445–450. [CrossRef]
36. Yang, S.; Vaagensmith, B.; Patra, D. Power Grid Contingency Analysis with Machine Learning: A Brief Survey and Prospects. In *Proceedings of the 2020 Resilience Week (RWS), Salt Lake City, UT, USA, 19–23 October 2020*; IEEE: Piscataway, NJ, USA, 2020; pp. 119–125. [CrossRef]
37. Al-Feilat, E.A.A.; El-Amin, I.; Bettayeb, M. Power system harmonic estimation: A comparative study. *Electr. Power Syst. Res.* **1994**, *29*, 91–97. [CrossRef]
38. Khokhar, S.; Zin, A.A.B.M.; Mokhtar, A.S.B.; Pesaran, M. A Comprehensive Overview on Signal Processing and Artificial Intelligence Techniques Applications in Classification of Power Quality Disturbances. *Renew. Sustain. Energy Rev.* **2015**, *51*, 1650–1663. [CrossRef]
39. Lin, H.; Sun, K.; Tan, Z.; Liu, C.; Guerrero, J.M.; Vasquez, J.C. Adaptive Protection Combined with Machine Learning for Microgrids. *IET Gener. Transm. Distrib.* **2019**, *13*, 770–779. [CrossRef]
40. Porawagamage, G.; Dharmapala, K.; Chaves, J.S.; Villegas, D.; Rajapakse, A. A Review of Machine Learning Applications in Power System Protection and Emergency Control: Opportunities, Challenges, and Future Directions. *Front. Smart Grids* **2024**, *3*, 1371153. [CrossRef]
41. Mishra, M.; Singh, J.G. A Comprehensive Review on Deep Learning Techniques in Power System Protection: Trends, Challenges, Applications and Future Directions. *Results Eng.* **2025**, *25*, 103884. [CrossRef]
42. Ren, C.; Xu, Y. Transfer Learning-Based Power System Online Dynamic Security Assessment: Using One Model to Assess Many Unlearned Faults. *IEEE Trans. Power Syst.* **2020**, *35*, 821–824. [CrossRef]

43. Yang, M.; Li, Y.; Li, J.; Lu, G.; Wang, H.; Fu, Y.; Fang, X. Transfer Learning-Based Updating Method of Transient Stability Assessment Model. *Energy Rep*. **2024**, *12*, 442–452. [CrossRef]
44. Arévalo-Soler, J.; Nahalparvari, M.; Groß, D.; Prieto-Araujo, E.; Norrga, S.; Gomis-Bellmunt, O. Small-Signal Stability and Hardware Validation of Dual-Port Grid-Forming Interconnecting Power Converters in Hybrid AC/DC Grids. *IEEE J. Emerg. Sel. Top. Power Electron*. **2025**, *13*, 809–826. [CrossRef]
45. IEEE Subsynchronous Resonance Task Force. First Benchmark Model for Computer Simulation of Subsynchronous Resonance. *IEEE Trans. Power Appar. Syst*. **1977**, *96*, 1565–1572. [CrossRef]
46. Shair, J.; Li, H.; Hu, J.; Xie, X. Power System Stability Issues, Classifications and Research Prospects in the Context of High-Penetration of Renewables and Power Electronics. *Renew. Sustain. Energy Rev*. **2021**, *145*, 111111. [CrossRef]
47. *Standard's IEEE*; Std 1547-2018. IEEE: New York, NY, USA, 2018. [CrossRef]
48. Teodorescu, R.; Liserre, M.; Rodriguez, P. *Grid Converters for Photovoltaic and Wind Power Systems*; Wiley-IEEE Press: Chichester, UK, 2011.
49. *Standard's IEC 61000-4-30:2015+AMD1:2021*; Electromagnetic Compatibility (EMC)—Part 4-30: Testing and Measurement Techniques—Power Quality Measurement Methods. International Electrotechnical Commission: Geneva, Switzerland, 2021.
50. CIGRE Working Group B4.72. *DC Grid Benchmark Models for System Studies*; Technical Brochure 804; CIGRE: Paris, France, 2020.
51. Kersting, W.H. *Distribution System Modeling and Analysis*; CRC Press: Boca Raton, FL, USA, 2001. [CrossRef]
52. Baran, M.E.; Wu, F.F. Network Reconfiguration in Distribution Systems for Loss Reduction and Load Balancing. *IEEE Trans. Power Deliv*. **1989**, *4*, 1401–1407. [CrossRef]
53. *Standard's IEC 60502-2:2014*; Power Cables with Extruded Insulation and Their Accessories for Rated Voltages from 1 kV (Um = 1.2 kV) up to 30 kV (Um = 36 kV)—Part 2: Cables for Rated Voltages from 6 kV (Um = 7.2 kV) up to 30 kV (Um = 36 kV). International Electrotechnical Commission: Geneva, Switzerland, 2014.
54. *Standard's IEC 61850-8-1:2011+AMD1:2020*; Communication Networks and Systems for Power Utility Automation—Part 8-1: Specific Communication Service Mapping (SCSM)—Mappings to MMS (ISO 9506-1 and ISO 9506-2) and to ISO/IEC 8802-3. International Electrotechnical Commission: Geneva, Switzerland, 2020.
55. Hung, D.Q.; Mithulananthan, N.; Bansal, R.C. Analytical Expressions for DG Allocation in Primary Distribution Networks. *IEEE Trans. Energy Convers*. **2010**, *25*, 814–820. [CrossRef]
56. Brown, T.; Hörsch, J.; Schlachtberger, D. PyPSA: Python for Power System Analysis. *J. Open Res. Softw*. **2018**, *6*, 4. [CrossRef]
57. *Standard's IEC 61089:1991*; Round Wire Concentric Lay Overhead Electrical Stranded Conductors. International Electrotechnical Commission: Geneva, Switzerland, 1991.
58. *IEEE Std 2800-2022*; IEEE Standard for Interconnection and Interoperability of Inverter-Based Resources (IBRs) Interconnecting with Associated Transmission Electric Power Systems. IEEE: New York, NY, USA, 2022. [CrossRef]
59. Chen, T.; Guestrin, C. XGBoost: A Scalable Tree Boosting System. In *Proceedings of the 22nd ACM SIGKDD International Conference on Knowledge Discovery and Data Mining, San Francisco, CA, USA, 13–17 August 2016*; IEEE: Piscataway, NJ, USA, 2016; pp. 785–794. [CrossRef]
60. Goodfellow, I.; Bengio, Y.; Courville, A. *Deep Learning*; MIT Press: Cambridge, MA, USA, 2016.
61. Hochreiter, S.; Schmidhuber, J. Long Short-Term Memory. *Neural Comput*. **1997**, *9*, 1735–1780. [CrossRef] [PubMed]
62. Snoek, J.; Larochelle, H.; Adams, R.P. Practical Bayesian Optimization of Machine Learning Algorithms. In *Proceedings of the Advances in Neural Information Processing Systems 25 (NIPS 2012), Lake Tahoe, NV, USA, 3–6 December 2012*; IEEE: Piscataway, NJ, USA, 2012; pp. 2951–2959.
63. Liu, J.; Shen, X.; Alcaide, A.M.; Yin, Y.; Leon, J.I.; Vazquez, S.; Wu, L.; Franquelo, L.G. Sliding Mode Control of Grid-Connected Neutral-Point-Clamped Converters via High-Gain Observer. *IEEE Trans. Ind. Electron*. **2022**, *69*, 4010–4021. [CrossRef]
64. Yin, Y.; Vazquez, S.; Marquez, A.; Liu, J.; Leon, J.I.; Wu, L.; Franquelo, L.G. Observer-Based Sliding-Mode Control for Grid-Connected Power Converters under Unbalanced Grid Conditions. *IEEE Trans. Ind. Electron*. **2022**, *69*, 517–527. [CrossRef]
65. Saltelli, A.; Ratto, M.; Andres, T.; Campolongo, F.; Cariboni, J.; Gatelli, D.; Saisana, M.; Tarantola, S. *Global Sensitivity Analysis: The Primer*; John Wiley & Sons: Chichester, UK, 2008.
66. Sobol', I.M. Global Sensitivity Indices for Nonlinear Mathematical Models and Their Monte Carlo Estimates. *Math. Comput. Simul*. **2001**, *55*, 271–280. [CrossRef]
67. Herman, J.; Usher, W. SALib: An Open-Source Python Library for Sensitivity Analysis. *J. Open Source Softw*. **2017**, *2*, 97. [CrossRef]
68. *IEC 60255-151:2009*; Measuring Relays and Protection Equipment—Part 151: Functional Requirements for Over/Under Current Protection. International Electrotechnical Commission: Geneva, Switzerland, 2009.
69. Quiñonero-Candela, J.; Sugiyama, M.; Schwaighofer, A.; Lawrence, N.D. (Eds.) *Dataset Shift in Machine Learning*; MIT Press: Cambridge, MA, USA, 2009.
70. Settles, B. *Active Learning Literature Survey*; Computer Sciences Technical Report 1648; University of Wisconsin–Madison: Madison, WI, USA, 2009.

71. Bryan, B.; Nichol, R.C.; Genovese, C.R.; Schneider, J.; Miller, C.J.; Wasserman, L. Active Learning for Identifying Function Threshold Boundaries. In Proceedings of the Advances in Neural Information Processing Systems 18 (NIPS 2005), Vancouver, BC, Canada, 5–8 December 2005.
72. Read, J.; Pfahringer, B.; Holmes, G.; Frank, E. Classifier Chains for Multi-Label Classification. *Mach. Learn.* **2011**, *85*, 333–359. [CrossRef]

Disclaimer/Publisher's Note: The statements, opinions and data contained in all publications are solely those of the individual author(s) and contributor(s) and not of MDPI and/or the editor(s). MDPI and/or the editor(s) disclaim responsibility for any injury to people or property resulting from any ideas, methods, instructions or products referred to in the content.